

1 **Assessment and prediction of dust emissions, deposition** 2 **and radiation forcing in Central Asia**

3 Ying Gan¹²³, Zhe Zhang^{1234*}, Wen Chu⁵, Jianli Ding⁶, Yuxin Ren¹²³

4 1College of Geography and Remote Sensing Sciences, Xinjiang University, Urumqi, 830046, China

5 2 Xinjiang Key Laboratory of Oasis Ecology, Xinjiang University, Urumqi, 830046, China

6 3 Key Laboratory of Smart City and Environment Modelling of Higher Education Institute, Xinjiang
7 University, Urumqi, 830046, China

8 4MNR Technology Innovation Center for Central Asia Geo-Information Exploitation and Utilization,
9 Urumqi, 830046, China

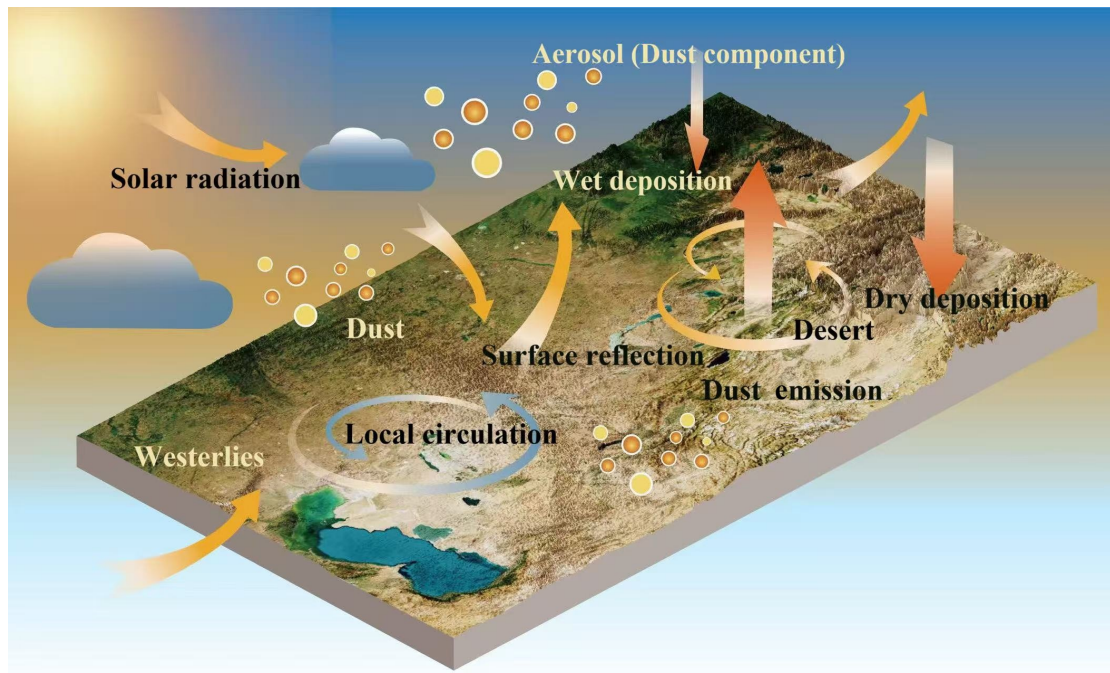
10 5College of Marine Technology, Faculty of Information Science and Engineering, Ocean University of
11 China; Qingdao, 266100

12 6Xinjiang Institute of Technology, Aksu, China;

13 **Correspondence to: zhangzhe_0110@yeah.net; Tel: +86 18799181249*

14 **Abstract.** Dust aerosols significantly influence climate by modulating radiative balance and cloud
15 processes. This study integrates MERRA-2 reanalysis data and the CMIP6 multi-model ensemble to
16 assess the spatiotemporal evolution of dust emissions, deposition, and associated radiative effects in
17 Central Asia from 1980 to 2100. Four SSP scenarios project that dust emissions in Central Asia exhibit
18 a high-emission, high-deposition pattern with primary sources exceeding $15 \mu\text{g}\cdot\text{m}^{-2}\cdot\text{s}^{-1}$. The deposition
19 area substantially exceeds the source area (maximum $>8 \mu\text{g}\cdot\text{m}^{-2}\cdot\text{s}^{-1}$). Cross-scenario analysis
20 demonstrates that dust emissions are highly sensitive to climate policy, with end-of-century emissions
21 in the SSP5-8.5 high-emission scenario increasing by 94.9% relative to the baseline period. In contrast,
22 emissions under the SSP1-2.6 low-carbon pathway vary by only 4.5%. Simulations using the SBDART
23 model show that aerosol direct radiative forcing (ADRF) from dust in Central Asia under clear-sky
24 conditions exhibits a vertical gradient, with cooling at the top of the atmosphere (TOA) and heating
25 within the atmosphere, yielding a net negative forcing at the TOA, with a minimum of $<-10 \text{ W/m}^2$ near
26 the Caspian Sea. Peak positive forcing within the atmosphere, observed in spring, reaches 10.0 W/m^2 .
27 Increased dust emissions reduce shortwave radiation at the surface by up to -20 W/m^2 . Ground-based
28 observations indicate seasonal variations in the dust-induced heating rate, with peak radiative forcing in
29 spring at Kashgar (93.0 W/m^2) and a maximum near-surface heating rate of 2.6 K/day . In contrast, the
30 near-surface heating rate at Issyk-Kul Lake in autumn (0.34 K/day) is approximately four times higher
31 than in spring (0.08 K/day).

32 **Graphical Abstract**



33

34 **Keywords:** Dust cycle; CMIP6 multi-model ensemble(MME); Direct radiative forcing of dust;
35 SBDART model

36 **1.Introduction**

37 Dust aerosols are a significant component of the tropospheric aerosol mass load, accounting for
38 approximately 50%, and profoundly impact the functioning of the Earth system (Mahowald et al., 2010;
39 Ramanathan et al., 2001). Their transboundary circulation process (lithosphere-atmosphere-cryosphere)
40 and interaction with the climate system have become cutting-edge research areas in Earth system
41 science. The release, transport, and deposition of dust aerosols not only involve multiple geospheres
42 but also substantially affect weather, climate, air quality, and human health upon entering the
43 atmosphere (Tegen et al., 2004; Penner et al., 2006; Pozzer et al., 2012).

44 Global annual dust emissions are substantial, ranging from approximately 1000 to 2150 Tg, with 30%
45 to 40% originating from arid regions of Asia (Tanaka and Chiba, 2006). Dust is transported across
46 continents by westerly wind circulation, significantly influencing the atmospheric radiation balance in
47 East Asia, North America, and the Arctic region (Wallace & Hobbs, 2006). Although studies have
48 confirmed that dust regulates the land-atmosphere energy budget through direct radiative forcing
49 (including scattering and absorption of shortwave and longwave radiation) and indirect effects (such as

50 altering precipitation efficiency as cloud condensation nuclei), significant uncertainty persists regarding
51 the vertical distribution of dust, the amplification mechanism of anthropogenic emissions, and their
52 regional climate feedback (IPCC, 2021).

53 Due to the challenges associated with dust observation, our understanding of the behavior of dust
54 throughout its life cycle remains insufficient, hindering a complete understanding and accurate
55 modeling of its complex mechanism of action (Kok et al. 2023, Rupakheti et al. 2023). Numerous
56 studies have used a variety of methods, including in situ observations, satellite remote sensing, and
57 model simulations, to thoroughly examine the spatiotemporal changes, optical properties, and radiative
58 forcing of dust aerosols(Wang et al. 2018, Song et al. 2021, Chen et al., 2022). For example, global
59 dust is primarily confined to the "dust belt," with approximately one-third originating from the Asian
60 region(Kok et al. 2023). Dai et al. utilized a variety of remote sensing and ground-based data to study
61 the sources, microphysical characteristics, and optical properties (Dai et al. 2022, Salvador et al. 2022).
62 Zhao et al. investigated the simulation of global and regional dust by 16 CMIP6 models in the
63 Atmospheric Model Intercomparison Project (AMIP) experiment and compared the results with
64 observational and reanalysis data (Zhao et al. 2023, Liu et al. 2024).

65 Model simulations provide information on the temporal and spatial changes of dust aerosols worldwide
66 and facilitate predictions of future trends (Li et al., 2021). Climate models, such as CMIP5 and CMIP6,
67 have enhanced our understanding of the main characteristics of dust aerosols. These models feature
68 increasing resolutions and increasingly complex physical processes and parameterizations,
69 demonstrating their ability to simulate dust events and processes on meso- to global scales (Zhao et al.,
70 2022). In particular, CMIP6 experiments have provided critical support for assessing the climatic
71 effects of dust emissions (Braconnot et al., 2021; Zhao et al., 2024). However, due to insufficient
72 resolution and simplified regional topography, the applicability of these global studies to the arid
73 regions of Central Asia remains limited, underscoring the need for high-resolution analyses at the
74 regional scale.

75 The arid regions of Central Asia, including Xinjiang in China, constitute the world's second-largest
76 dust source area, with distinctive surface characteristics leading to significant spatiotemporal variations
77 in dust emission fluxes (Shen et al., 2016). However, current research has primarily focused on the
78 spatiotemporal distribution and transport processes of dust (Li et al., 2022b; Tao et al., 2022), while key

79 aspects of the local dust lifecycle in this region—such as the long-term evolution of dust emission–
80 deposition budgets, the strong dependence of direct radiative forcing on dust vertical profiles, and
81 modal differences in dust–climate feedbacks under different carbon emission scenarios—remain poorly
82 understood. These knowledge gaps significantly constrain the reliability of climate models over Central
83 Asia, and uncertainties in radiative forcing estimates primarily stem from the lack of ground-based
84 validation due to the scarcity of observational stations (Brown et al., 2021; Wu and Boor, 2021).

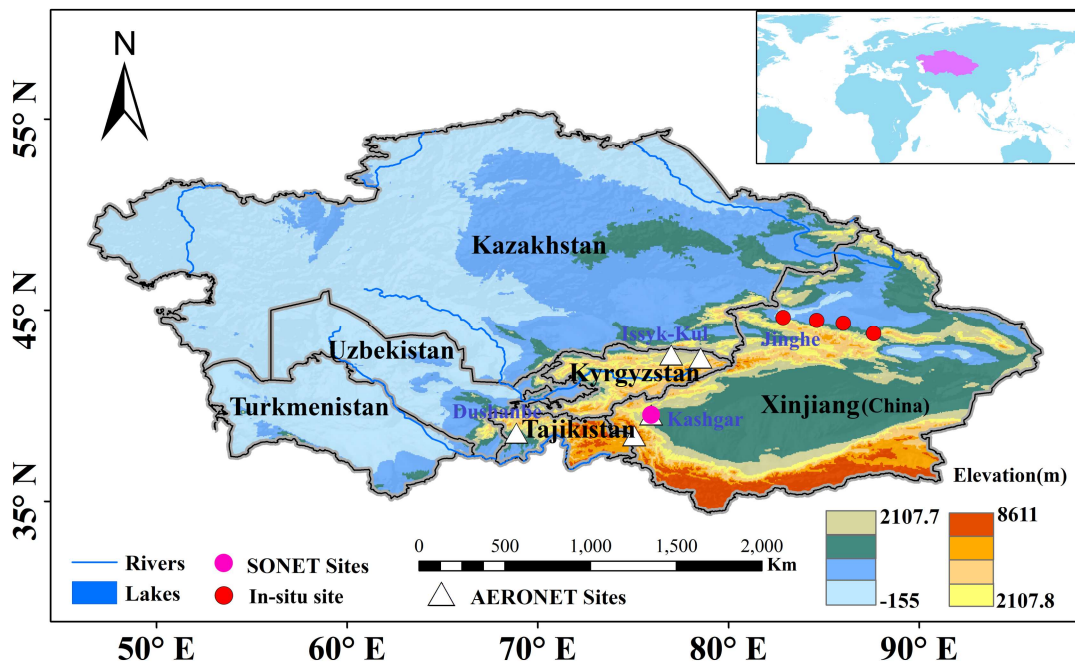
85 To overcome the above limitations, this study establishes a multi-source data integration framework
86 that systematically incorporates a full-chain analysis of “emission–deposition–radiation,” focusing on
87 the regional characteristics of the dust lifecycle over the arid regions of Central Asia. Unlike previous
88 studies that have mainly concentrated on the global scale (Kok et al., 2023; Zhao et al., 2022, 2023,
89 2024), this work achieves an integrated assessment at the regional scale and emphasizes the role of
90 observations in constraining model uncertainties. The specific innovations are reflected in three aspects:
91 (1) by combining MERRA-2 reanalysis with CMIP6 multi-model ensembles through statistical
92 downscaling, the long-term evolution of dust emission–deposition budgets and their scenario-based
93 differences in Central Asia are systematically characterized, thereby providing regionally refined
94 insights to complement global model results; (2) using the SBDART radiative transfer model together
95 with observational data from the SONET Asian Dust Monitoring Network and the Jinghe CE318
96 ground-based remote sensing site, the long-term trends of dust shortwave radiative forcing under clear-
97 sky conditions are quantified; and (3) by introducing the SARIMA statistical model, the short-term
98 evolution and risk implications of dust radiative effects are explored. This framework not only deepens
99 the understanding of dust physical mechanisms under the complex topography and local climate of
100 Central Asia but also provides new scientific support for improving regional climate simulations and
101 environmental risk management.

102 The structure of this paper is as follows. Section 2 presents the data sources, the downscaling method
103 for the CMIP6 dust budget, and the calculation method for clear-sky aerosol radiative forcing. Section
104 3 examines the detailed characteristics of the dust budget, projections of future changes, and the
105 radiative forcing of dust aerosols. Finally, the main conclusions and a discussion are presented in
106 Section 4.

107 **2. Data and Methods**

108 **2.1 Data sources**

109 The study area is situated between 35°–57°N and 48°–96°E, encompassing the five Central Asian
110 countries (Kazakhstan, Uzbekistan, Tajikistan, Turkmenistan, and Kyrgyzstan) and the Xinjiang region
111 of China (comprising both its northern and southern parts). This region, located in the hinterland of the
112 Eurasian continent, is characterized by a temperate continental climate with extreme aridity. The region
113 features a highly heterogeneous surface, with the Taklamakan Desert and the surrounding Gobi
114 (comprising over 40% of the study area) interspersed with mountain ranges, such as the Tianshan and
115 Pamir, forming a unique landform (Hetzl et al., 2002; Shen et al., 2016). As the world’s second-largest
116 source of dust, strong thermal and dynamic coupling drives intense dust activities (Zhang et al., 2020),
117 with emission hotspots concentrated in the Tarim Basin, the desiccated bed of the Aral Sea, and the
118 Kazakh steppe belt. This study focuses on the regional dust budget and radiative effects, utilizing
119 MERRA-2 reanalysis data, the CMIP6 multi-model ensemble, AERONET, SONET, and handheld
120 photometer data.



121

122 **Figure. 1 Location of the Study area.**

123 **2.1.1 Ground-based sun photometer data**

124 AERONET (AErosol RObotic NETwork) employs a CE-318 solar photometer to measure aerosol
125 optical depth (AOD) across eight bands in the range of 340–1640 nm and to derive microphysical
126 parameters, including single scattering albedo (SSA), refractive index (m), and particle size spectrum
127 (Holben et al., 1998; Holben et al., 2001). The Level 2 data exhibit an uncertainty of less than 5%. As
128 an internationally recognized standard for ground-based aerosol observations, its long-term stability
129 and algorithmic consistency provide reliable input for radiative forcing calculations (García et al.,
130 2012). The data used in this study are available from the AERONET website
131 (<https://aeronet.gsfc.nasa.gov/>).

132 The Chinese Academy of Sciences-led SONET (Sun-sky radiometer Observation NETwork) employs
133 the CE318-DP instrument to provide information on the chemical composition and vertical profile of
134 aerosols while adhering to AERONET’s stringent quality control procedures. The establishment of
135 SONET sites has effectively addressed gaps in AERONET’s spatial coverage in this source region (Li
136 et al., 2018). Cross-validation demonstrates that the correlation coefficient between SONET and
137 AERONET AOD is 0.98 (RMSE < 0.02), confirming a seamless integration of the two datasets (She et
138 al., 2024). The SONET data can be accessed from its official website (<http://www.sonet.ac.cn/>).

139 To supplement the limited temporal and spatial coverage of fixed stations, this study employs CE-318
140 and Microtops II handheld photometers to obtain transient AOD observations in the 550–870 nm band
141 (accuracy ± 0.01) for verifying the local applicability of satellite inversion products. By integrating
142 these multi-scale observational data, this study uses AERONET and SONET Level 2 data to provide
143 vertical profiles of aerosol optical-physical properties, calculate the direct radiative forcing of aerosols,
144 and validate satellite data on AOD and radiation flux in Central Asia (Supplementary Figure 1).

145 **2.1.2 MERRA-2 reanalysis data**

146 The MERRA-2 reanalysis data used in this study was developed by NASA’s Goddard Space Flight
147 Center. Its core is based on the GEOS-5 atmospheric circulation model and the ADAS-5.12.4
148 assimilation system. A global multi-element dataset with 72 vertical layers (surface to 80 km) and a
149 horizontal resolution of $0.625^\circ \times 0.5^\circ$ has been constructed from 1980 to the present by integrating
150 satellite remote sensing (MODIS/AVHRR aerosol optical thickness), ground-based observations

151 (soundings, aircraft observations), and GOCART aerosol chemical transport model output (Gelaro et
 152 al., 2017). In addition to covering variables related to clouds, radiation, and hydrological cycles, the
 153 coupled GOCART model distinguishes the interaction mechanisms of five aerosol types in this dataset:
 154 dust (DU), sea salt (SS), sulfate (SO₄), black carbon (BC), and organic carbon (OC). For the first time,
 155 the entire lifecycle of dust aerosols has been analyzed, providing key parameters such as monthly
 156 average dust emission flux, dry/wet deposition rate, particle size-classified loads, and single scattering
 157 albedo at 483.5 nm, ensuring physical consistency for quantifying dust radiative forcing (Buchard et al.,
 158 2017). Leveraging these data advantages, this study extracts radiation flux and dust cycle parameters
 159 under clear-sky conditions in Central Asia and systematically constructs a collaborative analysis
 160 framework for dust emissions, deposition, and radiative forcing.

161 2.1.3 CMIP6 model simulations

162 The Sixth Coupled Model Intercomparison Project (CMIP6) incorporates 112 climate models from 33
 163 institutions worldwide, with its multi-scenario simulations substantially exceeding those of previous
 164 studies in both breadth and depth (Eyring et al., 2016). To examine the decadal variations in dust
 165 emissions and dry and wet deposition in Central Asia, this study selected ten models from CMIP6
 166 based on data completeness. The selection criteria encompassed key variables in the dust cycle:
 167 monthly mean dust emission fluxes for the historical period (1980 – 2014) and for four Shared
 168 Socioeconomic Pathways (SSP1-2.6, SSP2-4.5, SSP3-7.0, and SSP5-8.5) from 2015 to 2100, as well as
 169 dust dry- and wet-deposition fluxes (the sum of which constitutes total deposition).

170 To ensure spatial consistency when comparing multi-source data, all model outputs were statistically
 171 downscaled and regridded to match the MERRA-2 reanalysis data (spatial resolution: 0.625° × 0.5°).
 172 This multi-model ensemble approach effectively captures uncertainties in climate responses while
 173 managing computational costs, thereby providing robust data support for analyzing the long-term
 174 evolution of the dust cycle in the arid region of Central Asia.

175 **Table.1 Overview of the models and simulations used in this study.**

Model	Nation	Resolution	Hist	SSP126	SSP245	SSP370	SSP585	Dust emission scheme	Model references
-------	--------	------------	------	--------	--------	--------	--------	----------------------	------------------

CESM2-WACCM	USA	1.25°×0.94°	3	1	5	3	5	Zender et al. (2003)	Danabasoglu et al. (2020)
CESM2	USA	1.25°×0.95°	11	3	3	3	3	Zender et al. (2003)	Wu et al. (2016)
CNRM-ESM2-1	France	1.25°×0.96°	3	5	10	5	5	Marticorena et al. (1997)	Séférian et al. (2019)
GFDL-ESM4	USA	1.25°×0.97°	1	1	1	1	1	Evans et al. (2016)	Dunne et al. (2020)
GISS-E2-1-G	USA	1.25°×0.98°	19	10	25	17	10	Ginoux et al. (2004)	Bauer et al. (2020)
GISS-E2-1-H	USA	1.25°×0.99°	10	5	5	1	5	Bauer and Koch.(2005)	Kelley et al. (2020)
GISS-E2-2-G	USA	1.25°×1.00°	5	5	5	5	5	Cakmur et al. (2006)	Rind et al. (2020)
MRI-ESM2-0	Japan	1.25°×1.01°	12	5	10	5	6	Tanaka and Chiba.(2005)	Yukimoto et al. (2019)
HadGEM3-GC31-LL	UK	1.875°×1.25°	5	3	4	2	3	Marticorena. (1995)	Williams et al. (2020)
UKESM1-0-LL	UK	1.25°×0.103°	3	5	5	3	4	Marticorena. (1995)	Senior et al. (2020)

176 2.2 Methodology

177 2.2.1 Delta statistical downscaling

178 Due to the limited original spatial resolution of the CMIP6 models (typically $\sim 1.25^\circ \times 1^\circ$), their direct
179 application to regional-scale dust cycle analyses may introduce systematic biases. Therefore, this study
180 employs the delta change factor method for statistical downscaling. At its core, this method separates
181 the historical biases of the climate models from the future change signal, enabling the reconstruction of
182 high-resolution climate variables (Maraun et al., 2010; Gutmann et al., 2014).

183 First, deviations during the baseline period are calculated by extracting the monthly mean dust
184 emission fluxes, $P_{m, his}$, from the historical simulations (1980–2014) of each CMIP6 model. These
185 fluxes are then matched to the MERRA-2 reanalysis observations, P_{obs} , for the same period to
186 determine the model's systematic deviation ratio.

$$187 \quad B_m = \frac{P_{m, his}}{P_{obs}} \quad (1)$$

188 where $\overline{P_{obs}}$ is the monthly average of the observation period, and Bm represents the spatial deviation of

189 model m in the reference period.

190 Second, the relative change factor for future scenarios is extracted, and the ratio of dust emissions for
191 each model during the future scenario period (2015–2100) relative to its historical simulation is
192 calculated.

$$193 \quad R_{m,fut} = \frac{P_{m,fut}}{P_{m,his}} \quad (2)$$

194 Among them, $P_{m,fut}$ is the monthly mean emission of model m in the future, and $P_{m,his}$ is the monthly
195 mean emission of model m over the historical period.

196 This approach decouples the historical deviations from the climate change signal, preserving the
197 physical response characteristics of CMIP6 to future climate forcings while enhancing simulation
198 accuracy at the regional scale through the incorporation of high-resolution observational data.
199 Compared to dynamic downscaling, it substantially reduces computational costs and is particularly
200 suitable for multi-model uncertainty quantification studies.

201 **2.2.2 SBDART Radiative Transfer Model Calculation of Direct Radiative Forcing of Aerosols**

202 The Santa Barbara DISORT Atmospheric Radiative Transfer (SBDART) model (Ricchiazzi et al., 1998)
203 was employed in this study to quantitatively assess the direct radiative effects of aerosols. SBDART
204 solves the atmospheric radiative transfer equation using the four-stream approximation. Its core
205 architecture comprises three modules: first, the discrete ordinates radiative transfer (DISORT) module,
206 which calculates the radiative fluxes in a 45-layer atmosphere (with a vertical resolution of 0.3 km);
207 second, the spectral parameterization module, which integrates the LOWTRAN-7 atmospheric
208 absorption spectrum and Mie scattering theory to cover the shortwave band from 0.25 to 4.0 μm ; and
209 third, the surface-atmosphere coupling module, which analyzes the radiative interactions between
210 surface albedo and atmospheric constituents such as water vapor and ozone.

211 This study is based on a comprehensive dataset, with key input parameters including the optical
212 properties (e.g., optical depth τ , single scattering albedo ω , asymmetry factor g) and the vertical
213 profiles of aerosols. These parameters were obtained from the solar photometer observation network in
214 Central Asia, which provides significant advantages in temporal and spatial resolution compared to
215 satellite retrieval products (Dubovik and King, 2000). To quantify the radiative forcing due to dust
216 aerosols, all simulations were conducted under clear-sky conditions, with the solar zenith angle fixed to

217 the seasonal mean value for the study area to ensure the comparability of regional radiative effects
 218 (Halthore et al., 2005). The aerosol direct radiative forcing (ADRF) was calculated using the standard
 219 approach, which determines the difference in net radiative flux with and without aerosols under cloud-
 220 free conditions. Specifically, the ADRF at a given altitude z , at the top of the atmosphere (TOA), at the
 221 surface (SFC), and in the atmosphere (ATM) can be defined as follows:

$$222 \quad NF_z = F_{z,down} - F_{z,up} \quad (3)$$

$$223 \quad ADRF_z = NF_z^{aer} - NF_z^{noaer} \quad (4)$$

$$224 \quad ADRF_{TOA} = NF_{TOA}^{aer} - NF_{TOA}^{noaer} \quad (5)$$

$$225 \quad ADRF_{SFC} = NF_{SFC}^{aer} - NF_{SFC}^{noaer} \quad (6)$$

$$226 \quad ADRF_{ATM} = ADRF_{TOA} - ADRF_{SFC} \quad (7)$$

$$227 \quad ADRF_{dust} = ADRF \times \left(\frac{DAOD}{AOD} \right) \quad (8)$$

228 Among them, $F_{z,down}$ and $F_{z,up}$ are the downward and upward radiative fluxes, NF_z^{aer} and NF_z^{noaer} are
 229 the net radiative fluxes with and without aerosols, and ADRF is the aerosol direct radiative forcing.

230 **2.2.3 SARIMA prediction model**

231 Given the non-stationarity and interannual cycle characteristics of the radiative forcing time series of
 232 Central Asian dust, this study employs the seasonal autoregressive integrated moving average
 233 (SARIMA) model for analysis. First, the augmented Dickey-Fuller test (ADF, $p < 0.05$) was used to
 234 confirm the non-stationarity of the series. A compound differencing strategy (first-order conventional
 235 difference $d=1$, first-order seasonal difference $D=1$, period $s=12$) was applied to eliminate trend and
 236 interannual fluctuations, resulting in a stationary residual series (KPSS test, $p > 0.1$).

237 The non-seasonal order ($p=2$, $q=1$) was determined based on the autocorrelation function (ACF) and
 238 partial autocorrelation function (PACF), while the seasonal order ($P=1$, $Q=1$) was optimized using grid
 239 search, yielding the final SARIMA(2,1,1)(1,1,1)₁₂ model (AIC=112.3, BIC=125.7). Model validation
 240 demonstrated a goodness of fit of $R^2=0.87$ for annual cycle dynamics, with a prediction error for
 241 extreme event peaks of less than 15%, confirming its effectiveness in analyzing non-stationary
 242 sequences (Sirisha et al., 2022).

243 **2.2.4 Linear Trend Method**

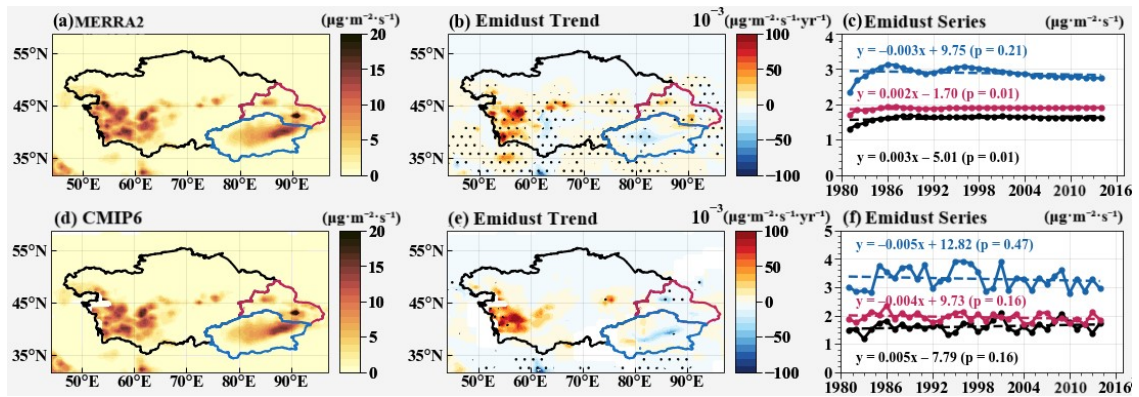
244 In this study, the ordinary least squares (OLS) method was used to perform linear regression on the
245 dust budget time series, with trend significance assessed via a two-tailed t-test. Spatial trends were
246 derived by conducting independent regressions at each grid point, with statistically significant results
247 ($p < 0.05$) indicated by stippling in the figures. Regional mean trends were calculated by regressing the
248 annual averages of grid values within specific regions (Central Asian countries, northern Xinjiang, and
249 southern Xinjiang). The regression slopes and corresponding p-values were annotated directly on the
250 time series plots.

251 **3. Results and Analysis**

252 **3.1 Spatial pattern and multi-mode prediction of dust emissions in Central Asia**

253 Figure 2 compares MERRA-2 observations with CMIP6 multi-model ensemble (MME) dust emissions
254 from 1980 to 2014. The historical spatial distribution from the 10 models is shown in Supplementary
255 Figure 2. Further analysis indicates that the observations are highly consistent with the MME
256 simulations, yielding a Taylor skill score (SS) of 0.87 and demonstrating strong performance in both
257 correlation and standard deviation. Dust emissions in the study area exhibit substantial temporal and
258 spatial variability. In terms of spatial distribution (Figure 2a), both datasets consistently identify the
259 three primary core emission sources in the Tarim Basin, the desiccated Aral Sea bed, and the Gobi
260 Desert, with maximum emission fluxes exceeding $15 \mu\text{g}\cdot\text{m}^{-2}\cdot\text{s}^{-1}$. Regarding the trends in dust
261 emissions (Figure 2b), those in the Aral Sea region have increased significantly ($>0.5 \mu\text{g}\cdot\text{m}^{-2}\cdot\text{s}^{-1} \text{ yr}^{-1}$)
262 over the past 34 years, whereas those in the Tarim Basin have slightly decreased ($\approx -0.3 \mu\text{g}\cdot\text{m}^{-2}\cdot\text{s}^{-1} \text{ yr}^{-1}$).
263 The Aral Sea region has experienced a 68% reduction in lake area since 1960, resulting in 54,000 km^2
264 of exposed lakebed (Wang et al., 2020). Under arid climatic conditions — with annual average
265 precipitation of less than 100 mm and potential evaporation exceeding 2000 mm—the dust emission
266 flux has increased significantly at a rate of approximately $0.5 \mu\text{g}\cdot\text{m}^{-2}\cdot\text{s}^{-1} \text{ yr}^{-1}$ over 34 years. In contrast,
267 the Tarim Basin has benefited from ecological restoration projects and increased precipitation during
268 the growing season (Fu et al., 2021), leading to a decrease in emission flux at a rate of $\approx -0.3 \mu\text{g}\cdot\text{m}^{-2}\cdot\text{s}^{-1}$
269 yr^{-1} . Time series analysis (Figure 2c) shows that overall dust emissions fluctuate gently without
270 significant annual trends. Dust emissions in the southern Tarim Basin of Xinjiang exhibit annual

271 increases and decreases, consistent with the spatial trend distribution. Dust emissions in northern
 272 Xinjiang are similar to those in Central Asia, with northern Xinjiang slightly higher than other Central
 273 Asian regions. This may be attributed to local differences in surface roughness and land use, reflecting
 274 regional disparities in emission characteristics.

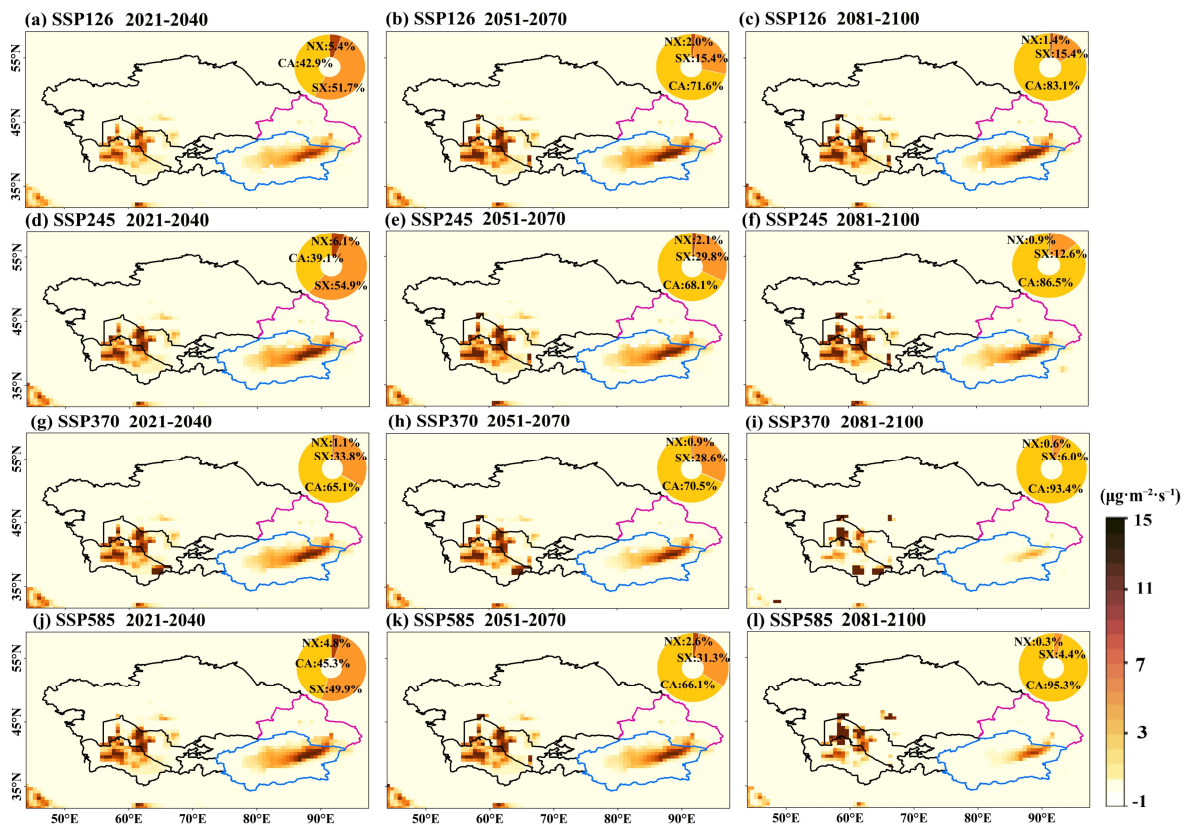


275 **Figure 2** Spatial distribution, linear trends, and time series of dust emissions from MERRA-2
 276 and the CMIP6 multi-model ensemble (MME) in Central Asia from 1980 to 2014. The red outline
 277 delineates Northern Xinjiang, the blue outline delineate Southern Xinjiang, and the black
 278 outlines denote the five Central Asian countries. Black dots in panels (b) and (e) mark regions
 279 significant at the 95% confidence level.

280 In the future projections, Figure 3 illustrates the relative changes in dust emissions over Central Asia
 281 under four radiative forcing scenarios (SSP1-2.6, SSP2-4.5, SSP3-7.0, and SSP5-8.5) for the near term
 282 (2021–2040), midterm (2051–2070), and long term (2081–2100), relative to the baseline period (1980–
 283 2014). The results reveal pronounced spatiotemporal heterogeneity in dust emissions across the region
 284 (absolute values are shown in Supplementary Figure 7). Under all scenarios, regions with high dust
 285 emission values (changes $>10 \mu\text{g}\cdot\text{m}^{-2}\cdot\text{s}^{-1}$ and relative change rates $>25\%$) are consistently located in
 286 the Aral Sea basin, Turkmenistan, and the eastern margin of the Tarim Basin. Overall, dust emission
 287 intensity shows a positive correlation with the magnitude of radiative forcing and increases
 288 progressively over time within each scenario (long term $>$ midterm $>$ near term). Specifically, in the
 289 Aral Sea region, near-term dust emissions range from $17.8 \mu\text{g}\cdot\text{m}^{-2}\cdot\text{s}^{-1}$ (SSP3-7.0) to $26.0 \mu\text{g}\cdot\text{m}^{-2}\cdot\text{s}^{-1}$
 290 (SSP2-4.5), with relatively small inter-scenario differences. However, as radiative forcing intensifies
 291 and time progresses, the rate of change in emissions rises from approximately 40% in the near term to
 292 about 70% in the midterm. Under the high-radiative-forcing scenario (SSP5-8.5), the long-term
 293 increase reaches its maximum, with an enhancement of about 94.9% relative to the reference
 294 period. This substantial increase is closely associated with the exposure of saline–alkaline sediments

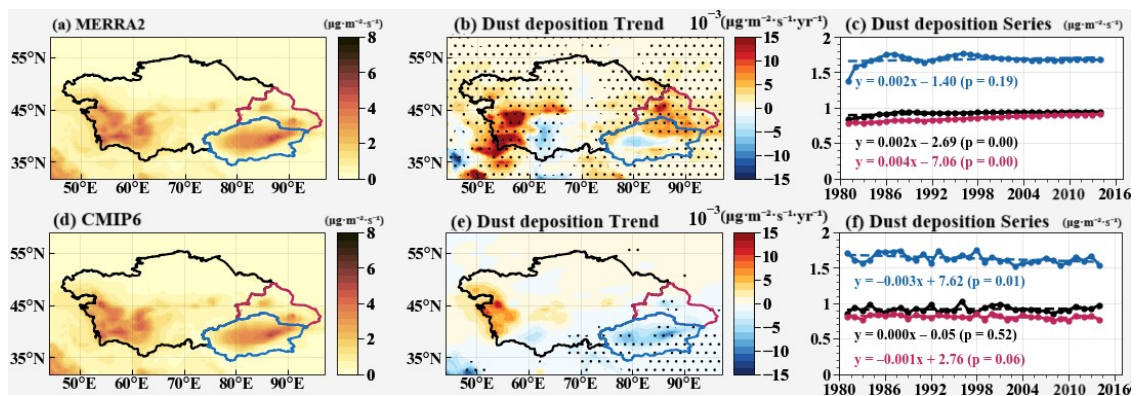
295 from the desiccated lakebed, soil loosening due to rising surface temperatures, and intensified wind
 296 erosion (Lioubimtseva and Cole, 2006).

297 In contrast, the Tarim Basin exhibits an overall decreasing trend in dust emissions, primarily driven by
 298 the combined effects of ecological restoration (a decadal NDVI increase of 0.12) and enhanced
 299 growing-season precipitation (Xu et al., 2019). Specifically, dust emissions decline by 18.7% under
 300 SSP2-4.5 and by 29.3% under SSP3-7.0. Under the SSP5-8.5 scenario, emissions decrease from 27.2
 301 $\mu\text{g}\cdot\text{m}^{-2}\cdot\text{s}^{-1}$ in the near term to 20.1 $\mu\text{g}\cdot\text{m}^{-2}\cdot\text{s}^{-1}$ in the long term, representing a reduction of
 302 approximately 26.1%, with the relative change rate showing a concurrent weakening trend. A regional
 303 comparison reveals substantial differences in climate response sensitivity: the emission increases over
 304 the Aral Sea region exhibit an exponential relationship with radiative forcing intensity ($R^2 = 0.93$),
 305 whereas those in southern Xinjiang show a slight declining tendency. This contrast highlights the
 306 potential role of human interventions in modulating dust processes across Central Asia.



307 **Figure. 3** Future changes in dust emissions across different periods. Spatial distribution of the
 308 relative changes in dust emissions over Central Asia under four CMIP6 multi-model ensemble
 309 (MME) SSP scenarios: panels (a–d) near term (2021–2040), (e–h) midterm (2051–2070), and (i–l)
 310 long term (2081–2100), relative to the historical period (2000–2014). The circular inset in the
 311 upper-right corner of each panel indicates the mean relative change rate (%) for the
 312 corresponding region.

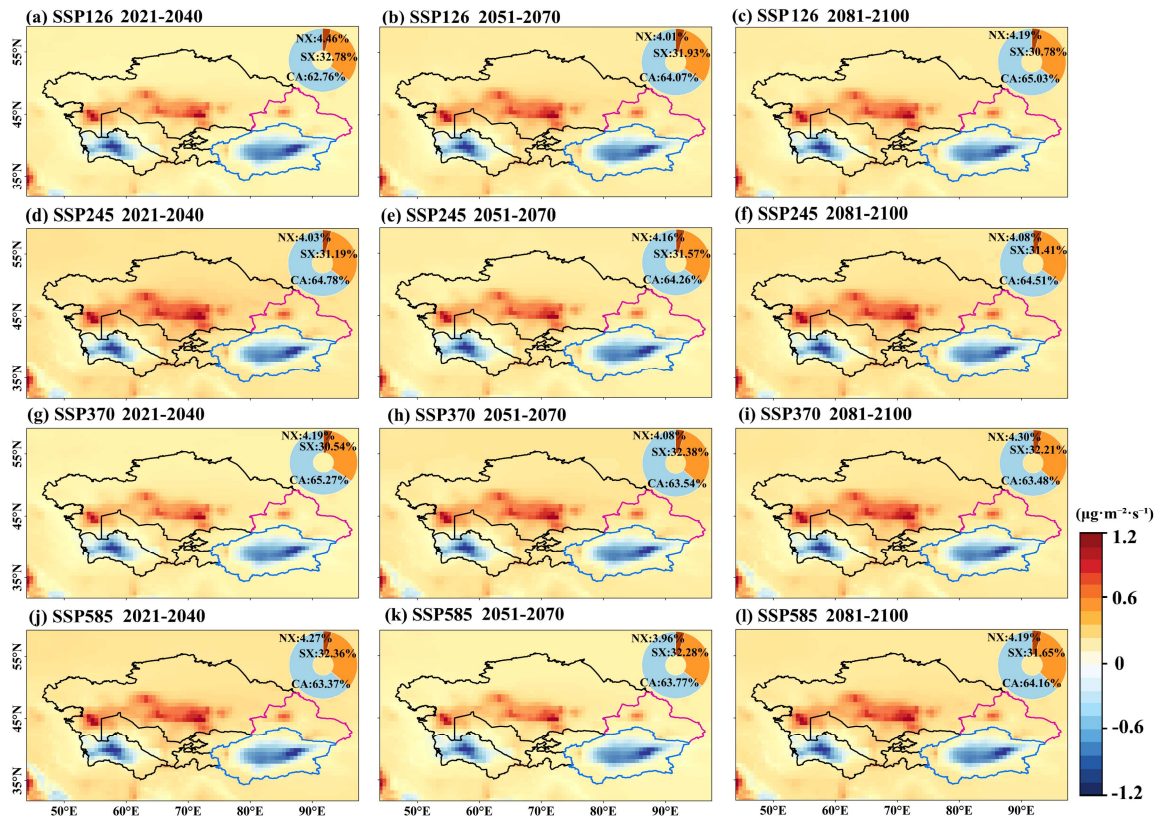
313 Dust emissions and deposition together constitute the complete dust mass balance process, with
 314 deposition representing the ultimate outcome of dust release. Once injected into the atmosphere, dust
 315 particles undergo dry deposition, driven primarily by gravitational settling, and wet deposition,
 316 facilitated by precipitation (the historical spatial distributions of dry and wet deposition from the ten
 317 models are shown in Supplementary Figures 3–4), thereby completing the material redistribution across
 318 the land–atmosphere interface (Marticorena and Bergametti, 1995; Shao et al., 2011). Quantitative
 319 assessments (Figure 4 and Supplementary Figures 5–6) indicate that the multi-model ensemble (MME)
 320 simulations agree well with observations in reproducing total dust deposition over Central Asia,
 321 yielding a Taylor skill score of 0.82. However, differences exist in the absolute magnitudes of
 322 deposition, and the observed trend intensity from MERRA-2 is substantially stronger than that
 323 simulated by the model ensemble. Spatially, regions with high deposition ($>5 \mu\text{g}\cdot\text{m}^{-2}\cdot\text{s}^{-1}$) largely
 324 coincide with emission hotspots, mainly concentrated in western Central Asia and the Tarim Basin in
 325 southern Xinjiang, confirming the spatially coupled “emission–deposition” mechanism of local dust
 326 processes. Trend analysis (Figure 4b) reveals that the Aral Sea and the eastern Caspian region exhibit
 327 the strongest positive trends ($\Delta S = +0.15 \mu\text{g}\cdot\text{m}^{-2}\cdot\text{s}^{-1}$), whereas southern Xinjiang is dominated by a
 328 negative trend ($\Delta S = -0.10 \mu\text{g}\cdot\text{m}^{-2}\cdot\text{s}^{-1}$). Temporally (Figure 4c), the observational data show a slight
 329 increasing trend in dust deposition flux over Central Asia during 1980–2014, with a rate of 0.002
 330 $\mu\text{g}\cdot\text{m}^{-2}\cdot\text{s}^{-1} \text{ yr}^{-1}$, while the MME simulations indicate a weak decreasing trend of $-0.003 \mu\text{g}\cdot\text{m}^{-2}\cdot\text{s}^{-1} \text{ yr}^{-1}$
 331 over Xinjiang. This discrepancy between observations and simulations may stem from uncertainties in
 332 model representations of boundary-layer dynamics and precipitation microphysics in arid Central Asia,
 333 particularly in the quantification of dust wet deposition efficiency, which still requires improvement.



334
 335 **Figure. 4 Spatial distribution, linear trends, and temporal variations of total dust deposition**
 336 **(dry + wet) over Central Asia from 1980 to 2014, based on MERRA-2 observations and CMIP6**
 337 **multi-model ensemble (MME) simulations. Red shading highlights northern Xinjiang, blue**

338 shading indicates southern Xinjiang, and black outlines denote the five Central Asian countries.
339 In panels (b) and (e), black dots denote regions where the trends are statistically significant at the
340 95% confidence level ($p < 0.05$).

341 Figure 5 illustrates the projected relative changes in dust deposition under four SSP scenarios across
342 different time periods (future changes in dry and wet deposition are shown in Supplementary Figures
343 9–10). Unlike the source-concentrated distribution of dust emissions, the spatial extent of deposition
344 extends outward, mainly covering southwestern Central Asia, the southeastern margin of the Tarim
345 Basin, and the Junggar Basin, with maximum deposition fluxes exceeding $8 \mu\text{g}\cdot\text{m}^{-2}\cdot\text{s}^{-1}$. This forms a
346 distinct spatial pattern characterized by a “deposition domain > emission source.” From a temporal
347 perspective, near-term (2021–2040) mean deposition ranges from $9.3 \mu\text{g}\cdot\text{m}^{-2}\cdot\text{s}^{-1}$ (SSP5-8.5) to 10.4
348 $\mu\text{g}\cdot\text{m}^{-2}\cdot\text{s}^{-1}$ (SSP2-4.5), whereas long-term (2081–2100) values vary between $9.6 \mu\text{g}\cdot\text{m}^{-2}\cdot\text{s}^{-1}$ (SSP3-7.0)
349 and $10.0 \mu\text{g}\cdot\text{m}^{-2}\cdot\text{s}^{-1}$ (SSP1-2.6). The overall change is less than $1 \mu\text{g}\cdot\text{m}^{-2}\cdot\text{s}^{-1}$, corresponding to a
350 variation amplitude below 12%, and the relative change rate remains stable across all scenarios,
351 suggesting that future radiative forcing exerts limited influence on dust deposition processes. This
352 phenomenon may be attributed to the compensatory effects between dry and wet deposition. In
353 southern Xinjiang, changes in the precipitation regime under moderate-to-high radiative forcing lead to
354 a gradual decline in dry deposition flux at a rate of approximately $0.2 \mu\text{g}\cdot\text{m}^{-2}\cdot\text{s}^{-1} \text{ yr}^{-1}$. Conversely, in
355 western Central Asia, enhanced near-surface wind speeds resulting from reduced surface roughness
356 increase dry deposition, while the spatiotemporal stability of wet deposition mitigates fluctuations in
357 total deposition.

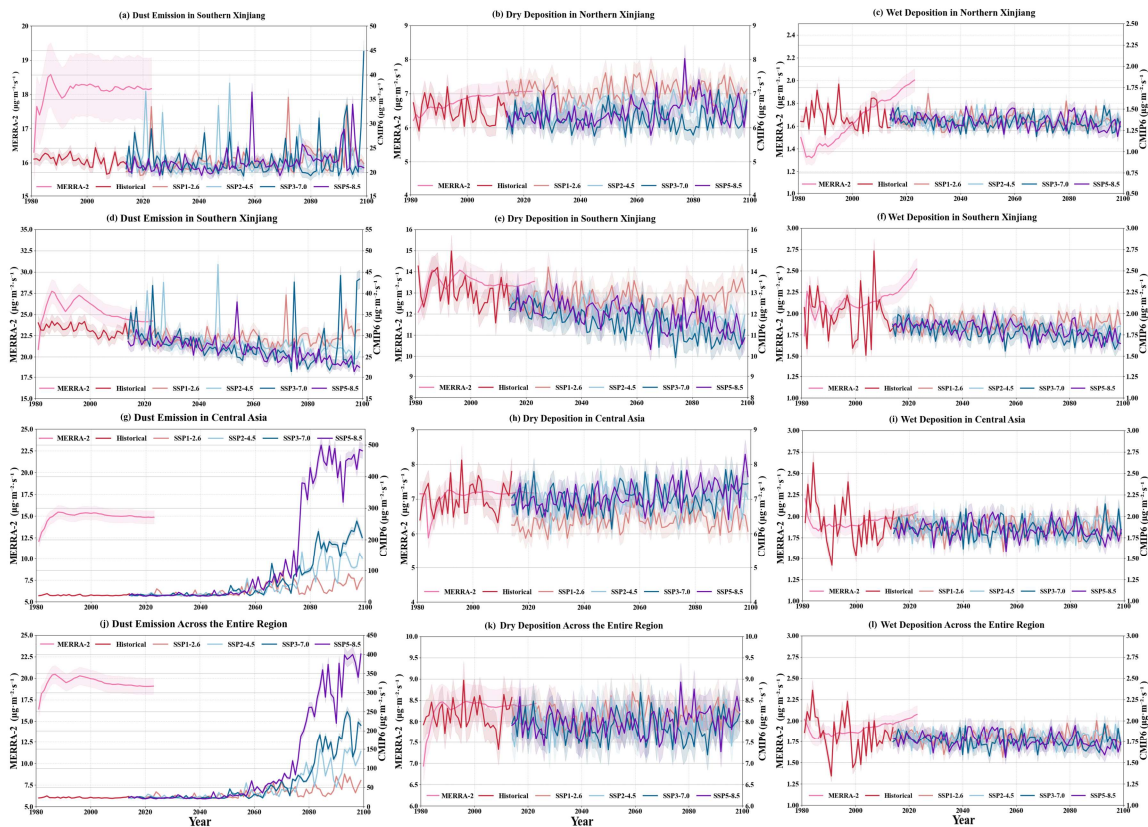


358 **Figure. 5 Spatial distribution of relative changes in total dust deposition over Central Asia under**
 359 **four CMIP6 multi-model ensemble (MME) SSP scenarios for different future periods: panels (a–**
 360 **d) near term (2021–2040), (e–h) midterm (2051–2070), and (i–l) long term (2081–2100), relative**
 361 **to the historical period (2000–2014). The circular inset in the upper-right corner of each panel**
 362 **indicates the mean relative change rate (%) for the corresponding region.**

363 To more accurately assess the trend simulation performance of the dust cycle, we constructed time
 364 series of dust emissions and wet and dry deposition from 1980 to 2100 based on MERRA-2 reanalysis
 365 data and CMIP6 multi-model ensemble (MME) simulations (see Fig. 6). Overall, the simulations
 366 indicate that dust emissions in Xinjiang remain relatively stable over the next 120 years. In contrast, in
 367 the five Central Asian countries—particularly under high-radiative-forcing scenarios (e.g., SSP3-7.0,
 368 SSP5-8.5)—dust emissions increase significantly (e.g., up to 94.9% under SSP5-8.5) between 2081 and
 369 2100, accompanied by a fluctuating but gradual rise. By comparison, dust deposition (both dry and wet)
 370 exhibits a smoother trend with lower volatility.

371 In the specific analyses, MERRA-2 dust emissions show a smooth trend, with averages of 30
 372 $\mu\text{g}\cdot\text{m}^{-2}\cdot\text{s}^{-1}$ in the Tarim Basin and 15 $\mu\text{g}\cdot\text{m}^{-2}\cdot\text{s}^{-1}$ in other regions. In contrast, MME-simulated
 373 emissions exhibit slight fluctuations, with peaks exceeding 45 $\mu\text{g}\cdot\text{m}^{-2}\cdot\text{s}^{-1}$ at certain times. Some
 374 deviations are observed in the temporal variability between the two datasets. The volatility of dust dry
 375 deposition is relatively low, with a slope of less than 0.1, indicating a smooth process. Additionally,

376 neither dry nor wet deposition shows significant long-term volatility. Wet deposition exhibits slight
 377 deviations in northern Xinjiang but remains relatively smooth in other regions, with an average flux of
 378 approximately $1.5 \mu\text{g}\cdot\text{m}^{-2}\cdot\text{s}^{-1}$ and an overall slope of less than 0.2, indicating limited variation. Notably,
 379 MERRA-2 wet deposition data show a marked increase in the northern border region around 2000,
 380 likely related to the assimilation of MODIS satellite and other observations in MERRA-2. Therefore,
 381 MERRA-2 data from 2000 to 2014 were selected for model calibration to ensure simulation accuracy.
 382 In summary, although future dust emissions vary substantially under different climate scenarios, the
 383 overall dust deposition process remains relatively stable. The MERRA-2 and MME simulation results
 384 exhibit spatial and temporal differences across regions.



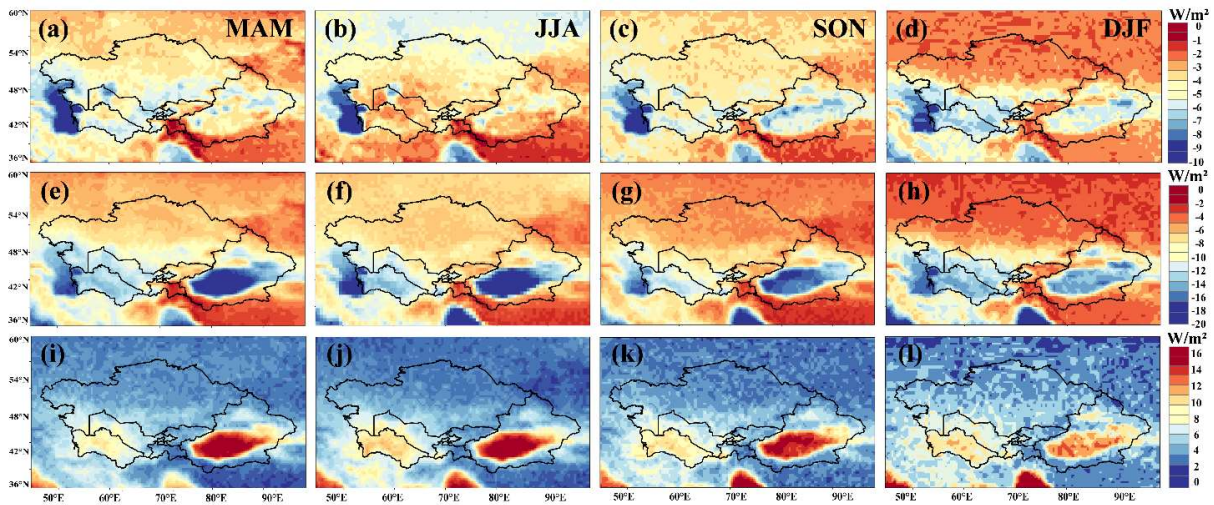
385 **Figure. 6** Time evolution of the dust budget. Dust emissions, dry and wet deposition ($\mu\text{g}\cdot\text{m}^{-2}\cdot\text{s}^{-1}$)
 386 for panels (a–c) Northern Xinjiang, (d–f) Southern Xinjiang, (g–i) Central Asia, and (j–l) the
 387 entire study region. Results are from the CMIP6 multi-model ensemble (MME; 1980–2100) and
 388 MERRA-2 (1980–2023).

389 3.3.1 Monthly average changes in direct radiative forcing by dust aerosols

390 Based on the quantitative characterization of dust emission sources and deposition processes described
 391 above, further investigation is needed to elucidate the perturbation mechanisms of dust aerosols on the
 392 surface–atmosphere energy balance. This study quantifies the radiative impacts of Central Asian dust

393 aerosols at various spatial and temporal scales through shortwave aerosol direct radiative forcing
394 (ADRF) derived from MERRA-2 observations under clear-sky conditions from 1980 to 2023. As
395 shown in Figure 7a–d, the top-of-atmosphere (TOA) radiative forcing exhibits substantial spatial
396 heterogeneity. Overall, the negative forcing reaches its lowest values ($<-10 \text{ W/m}^2$) in the Caspian Sea
397 region, followed by the Tarim Basin and the Aral Sea region ($<-8 \text{ W/m}^2$), confirming that dust aerosols
398 exert a significant cooling effect by enhancing shortwave reflection. Seasonal analysis reveals that the
399 negative TOA forcing intensity decreases in the order spring (-3.32 W/m^2) > summer (-3.21 W/m^2) >
400 autumn (-3.07 W/m^2) > winter (-1.94 W/m^2), which aligns closely with the seasonal characteristics of
401 dust activity. In spring, strong surface wind erosion across Central Asia drives intense dust emissions,
402 resulting in high atmospheric dust loading and optical depth and, consequently, the strongest radiative
403 forcing. Although summer convective activity can transport dust to higher altitudes, weakened near-
404 surface wind erosion reduces the overall dust burden relative to spring (Ginoux et al. 2012). During
405 autumn and winter, dust activity declines markedly, yielding the weakest annual radiative forcing.

406 The spatial pattern of surface (SFC) radiative forcing (Figure 7e–h) exhibits stronger negative values,
407 with two pronounced cooling centers over the Tarim Basin and southwestern Central Asia, where
408 shortwave radiation loss peaks at -20 W/m^2 . This arises from the combined scattering and absorption
409 effects of dust particles on incoming solar radiation (Li et al., 2022a), which substantially reduce
410 surface net radiation, thereby diminishing sensible heat flux and evaporation processes and suppressing
411 the transfer of heat and water vapor from the surface to the atmosphere. The atmospheric radiative
412 forcing (ADRF) exhibits a spatial pattern consistent with those at the TOA and SFC but features
413 positive values (10.02 W/m^2 in spring and 9.89 W/m^2 in summer), indicating the energy redistribution
414 role of dust aerosols in trapping solar energy within the atmospheric system via shortwave
415 absorption. This vertical gradient of “surface cooling and atmospheric heating” induces substantial
416 changes in the regional thermodynamic structure (Kok et al. 2017). On one hand, surface cooling
417 diminishes sensible heat flux and evaporation, thereby exacerbating moisture deficits in Central Asia’s
418 arid regions and limiting vegetation growth and agricultural productivity. On the other hand,
419 atmospheric heating strengthens the temperature gradient from the boundary layer to the free
420 troposphere, enhancing the potential for deep convection, which could intensify the frequency and
421 severity of spring–summer dust storms and modify regional precipitation patterns and extreme weather



423 **Figure. 7** Seasonal spatial distribution of clear-sky shortwave aerosol direct radiative forcing
 424 (ADRF) due to dust aerosols in Central Asia (1980–2023): at the top of the atmosphere (panels a–
 425 d), at the surface (e–h), and in the atmosphere (i–l).

426 3.3.2 Refinement of aerosol direct radiative forcing in dusty weather

427 Following a thorough examination of the spatial distribution characteristics of atmospheric dust aerosol
 428 direct radiative forcing (DRF) derived from MERRA-2 reanalysis data, this study further refines the
 429 analysis by simulating the radiative effects of dust aerosols at representative Central Asian sites using
 430 the Santa Barbara DISORT Atmospheric Radiative Transfer (SBDART) model (Figure 8).

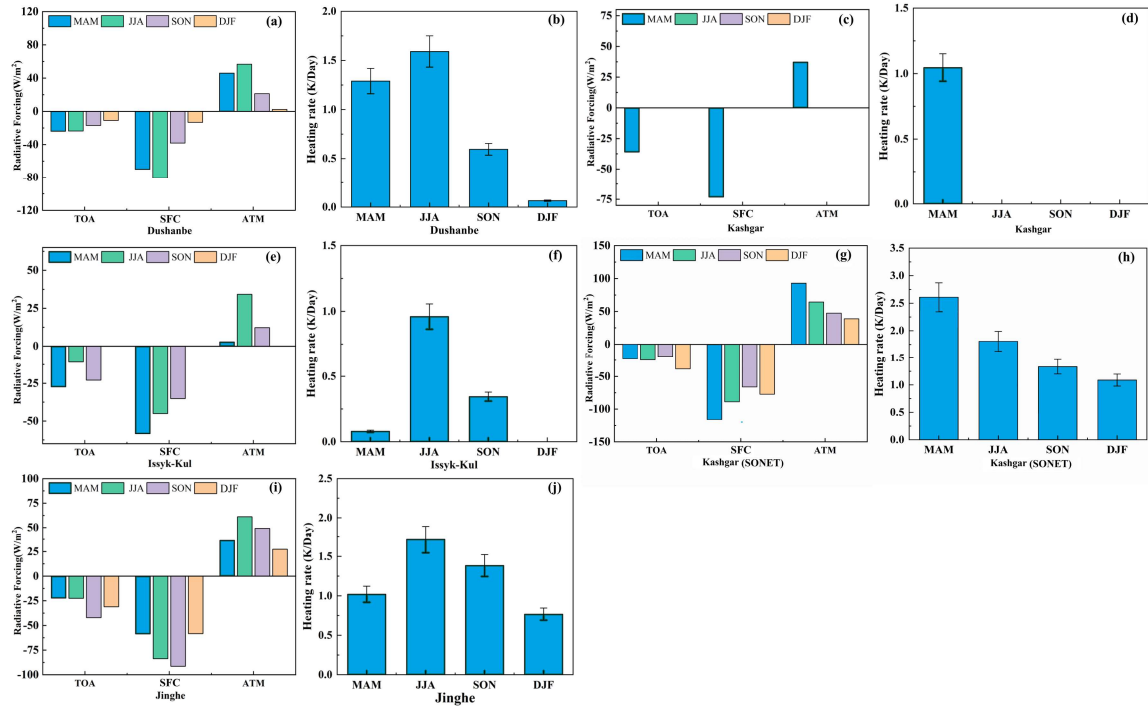
431 These simulations are based on ground-based observations from 2011 to 2023, encompassing
 432 AERONET sites at Dushanbe (Tajikistan; representing the Central Asian interior), Issyk-Kul
 433 (Kyrgyzstan; representing high-altitude lake regions), and Kashgar (Xinjiang, China; representing the
 434 Tarim Basin dust source region), as well as the SONET site at Kashgar and our self-established Jinghe
 435 site (Xinjiang, China; representing the Gobi–desert transitional zone). Although the number of sites is
 436 limited, their spatial distribution covers the primary dust source regions and representative surface
 437 types, thereby achieving a degree of regional representativeness. This section focuses on site-scale
 438 aerosol direct radiative forcing (ADRF), with particular emphasis on atmospheric radiative forcing
 439 (ATM) and the associated atmospheric heating rates, to provide a detailed understanding of the
 440 thermodynamic effects of dust on the atmospheric column.

441 Observations indicate that ADRF exhibits distinct seasonal variations. At the Dushanbe, Issyk-Kul, and
 442 Jinghe sites, atmospheric radiative forcing peaks in summer (56.72, 34.22, and 61.17 W/m²,

443 respectively) and declines to annual minima in winter (approximately 2.33 W/m^2 at Dushanbe and
444 27.36 W/m^2 at Jinghe), consistent with the frequent summer dust events in western Central Asia driven
445 by westerly circulation (Li et al., 2022b). Notably, the Kashgar site exhibits a unique spring-dominated
446 pattern, with a maximum ADRF of 92.99 W/m^2 , which may be associated with the Tarim Basin's
447 specific dust emission mechanisms, involving springtime snowmelt that exposes bare surfaces and
448 interacts with intense Mongolian cyclone activity.

449 Changes in the atmospheric heating rate maintain a clear positive correlation with ADRF, confirming
450 the central role of radiation absorption by dust aerosols. The peaks in heating rates at all sites occur
451 during the active dust period: those at Dushanbe (1.29 K/day in summer) and Jinghe (1.72 K/day in
452 summer) align with westerly transport paths, while the anomalously high value at Kashgar in spring
453 (2.61 K/day) corresponds to significant sand uplift events in the Taklamakan Desert. Notably, the
454 heating rate at Issyk-Kul in spring (0.08 K/day) is substantially lower than that in autumn (0.34 K/day),
455 possibly due to the site being shielded by mountainous terrain, which limits vertical dust transport in
456 spring. This may also affect the accuracy of the results, given the relative scarcity of observational data
457 at the Issyk-Kul site. This study reveals that the spatial and temporal divergence of regional radiative
458 effects is primarily controlled by two major factors: (1) seasonal modulation of emission intensity in
459 dust source regions, exemplified by enhanced dust transport from westerly jets to the Aral Sea basin in
460 summer, and (2) modulation of localized atmospheric boundary layer processes, typically manifested as
461 differences in thermal response between a mountainous site (Issyk-Kul) and a basin site (Kashgar).

462 These findings provide essential observational constraints for improving dust-radiation
463 parameterization schemes in regional climate models.



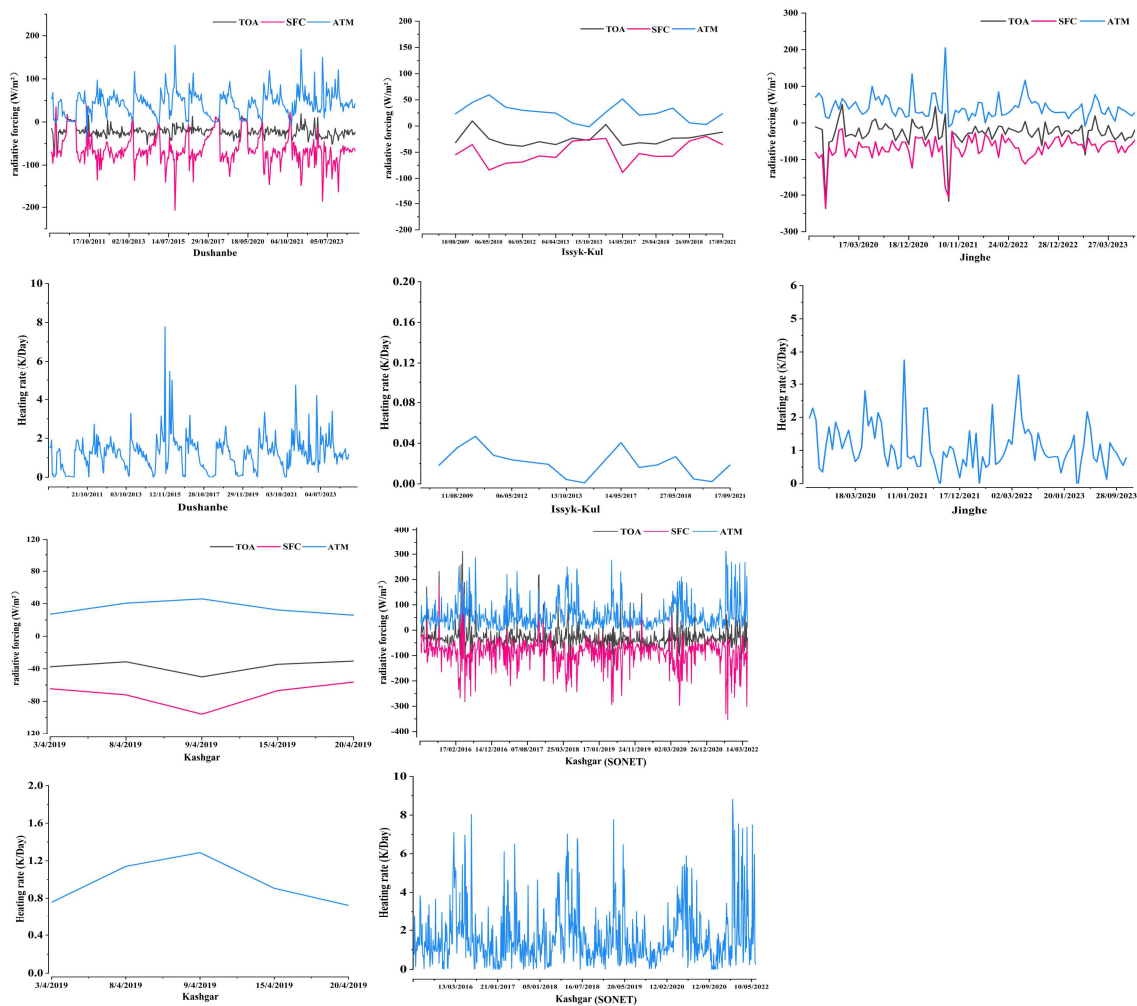
464

465 **Figure. 8** Seasonally averaged shortwave radiative forcing and atmospheric heating rate
 466 (including direct radiative forcing at the top of the atmosphere (TOA), the surface (SUR), and
 467 the atmosphere (ATM)) for dust aerosols at stations in Central Asia.

468 Figure 9 provides a further refinement of the aerosol direct radiative forcing (ADRF) at the sites,
 469 revealing that the daily variations in radiative forcing at the top of the atmosphere (TOA), surface
 470 (SFC), and throughout the atmosphere exhibit a clear pattern of temporal divergence. The ADRF time
 471 series at each site shows a differentiated response: at Dushanbe (2011–2023), typical characteristics of
 472 inland Central Asia are evident, with TOA and SFC forcing oscillating within ± 200 W/m² and
 473 atmospheric heating rates peaking at 8 K/day. Short-term variations are primarily driven by intermittent
 474 dust transport induced by disturbances in the westerly jet. At the Jinghe site, a generally stable trend is
 475 observed, punctuated by transient episodes of strong negative forcing (SFC < -250 W/m²) during
 476 extreme dust events. The Kashgar site displays pronounced temporal variability, with TOA/SFC
 477 forcing ranging from ± 400 W/m² and heating rates between 0 and 8 K/day during 2016–2022,
 478 including high-frequency oscillations in the afternoons of spring and summer. This behavior is directly
 479 linked to the Tarim Basin’s unique “afternoon mixed-layer development–vertical dust uplift”
 480 mechanism (Nakamae and Takemi, 2022), which may further increase the likelihood of regional dust
 481 events by intensifying local convective activity.

482 Notably, recent observations indicate enhanced irregular variability in ADRF during 2020–2023, which

483 may be attributed to the combined effects of changing surface cover and the increased frequency of
 484 extreme weather events in arid Central Asia, resulting in heightened instability in dust emissions and
 485 boundary-layer thermodynamic responses. At Kashgar, pronounced day-to-day fluctuations ($\Delta\text{ADRF} >$
 486 50 W/m^2) reveal the sensitive feedback of aerosol loading from the Taklamakan Desert source region
 487 on boundary-layer thermodynamics. These high-resolution observational results suggest that transient
 488 perturbations in dust radiative effects may alter boundary-layer stability and convective potential,
 489 thereby influencing precipitation variability and ecosystem stability in arid Central Asia. Such findings
 490 provide critical observational constraints for dust–radiation parameterizations in regional climate
 491 models.



492 **Figure. 9** Shortwave direct radiative forcing and atmospheric heating rates at Central Asian sites
 493 (AERONET/SONET data). Upper panels (a, b, c, g, h) show forcing at the top of the atmosphere
 494 (TOA), surface (SFC), and in the atmosphere (ATM); lower panels (d, e, f, i, j) show the
 495 corresponding atmospheric heating rates for (a, d) Dushanbe, (b, e) Issyk-Kul, (c, f) Jinghe, and
 496 (g–j) Kashgar.

497 4. Conclusion and discussion

498 4.1 Conclusion

499 Dust aerosols play a pivotal role in the climate system, characterized by substantial complexity and
500 regional variability. This study compares the spatial distributions and temporal trends of dust emissions
501 and deposition in Central Asia, while projecting future trends based on MERRA-2 reanalysis data and
502 dust cycle simulations from the CMIP6 multi-model ensemble (MME). Comparative analysis from
503 1980 to 2014 reveals strong consistency between the reanalysis data and MME simulations. The
504 primary dust emission hotspots are the Tarim Basin, the desiccated Aral Sea region, and the Gobi
505 Desert, where maximum emission fluxes exceed $15 \mu\text{g}\cdot\text{m}^{-2}\cdot\text{s}^{-1}$. Over the 34-year period, dust emissions
506 in the Aral Sea region have increased significantly ($>0.5 \mu\text{g}\cdot\text{m}^{-2}\cdot\text{s}^{-1}\cdot\text{yr}^{-1}$), whereas emission fluxes in
507 the Tarim Basin exhibit a declining trend at a rate of $\approx -0.3 \mu\text{g}\cdot\text{m}^{-2}\cdot\text{s}^{-1}\cdot\text{yr}^{-1}$.

508 Regarding short-, medium-, and long-term projections, regions with high dust emission values in
509 Central Asia remain stable in the Aral Sea hinterland, Turkmenistan, and along the eastern margin of
510 the Tarim Basin. Short-term emissions in the Aral Sea region range from 17.8 to $26.0 \mu\text{g}\cdot\text{m}^{-2}\cdot\text{s}^{-1}$,
511 exhibiting minimal inter-scenario variation; however, under high-radiative-forcing scenarios (e.g.,
512 SSP5-8.5), long-term dust emissions in Central Asia increase to $387.1 \mu\text{g}\cdot\text{m}^{-2}\cdot\text{s}^{-1}$, representing an
513 enhancement of up to 94.9% relative to the reference period. In contrast, long-term emissions in the
514 Tarim Basin demonstrate a declining trend, with reductions ranging from 18.7% under the SSP2-4.5
515 scenario to 29.3% under the SSP3-7.0 scenario. Particularly under the SSP5-8.5 scenario, short-term
516 emissions stand at $27.2 \mu\text{g}\cdot\text{m}^{-2}\cdot\text{s}^{-1}$, decreasing to $20.1 \mu\text{g}\cdot\text{m}^{-2}\cdot\text{s}^{-1}$ in the long term—a reduction of
517 26.1%.

518 Regions with high dust deposition values ($>5 \mu\text{g}\cdot\text{m}^{-2}\cdot\text{s}^{-1}$) overlap substantially with emission hotspots.
519 Trend analysis reveals that the Aral Sea and the eastern Caspian region exhibit the strongest positive
520 trends ($\Delta S = +0.15 \mu\text{g}\cdot\text{m}^{-2}\cdot\text{s}^{-1}$), whereas southern Xinjiang shows a negative trend ($\Delta S = -0.10$
521 $\mu\text{g}\cdot\text{m}^{-2}\cdot\text{s}^{-1}$). Under the four future scenarios, dust deposition influences extend across southwestern
522 Central Asia, the southeastern margin of the Tarim Basin, and the Junggar Basin, with maximum fluxes
523 exceeding $8 \mu\text{g}\cdot\text{m}^{-2}\cdot\text{s}^{-1}$. Mean values in the near term (2021–2040) range from $9.3 \mu\text{g}\cdot\text{m}^{-2}\cdot\text{s}^{-1}$ (SSP5-
524 8.5) to $10.4 \mu\text{g}\cdot\text{m}^{-2}\cdot\text{s}^{-1}$ (SSP2-4.5), and from $9.6 \mu\text{g}\cdot\text{m}^{-2}\cdot\text{s}^{-1}$ (SSP3-7.0) to $10.0 \mu\text{g}\cdot\text{m}^{-2}\cdot\text{s}^{-1}$ (SSP1-2.6) in
525 the long term (2081–2100), with an overall variation of less than 12%.

526 The aerosol direct radiative forcing (ADRF) due to dust aerosols under clear skies in Central Asia
527 exhibits notable spatial patterns. Overall, the top-of-atmosphere (TOA) radiative forcing is negative,
528 with the lowest values observed in the Caspian Sea region (<-10 W/m²), followed by the Tarim Basin
529 and the Aral Sea region (<-8 W/m²). The seasonal TOA forcing minima decrease in the order spring ($-$
530 3.32 W/m²) $>$ summer (-3.21 W/m²) $>$ autumn (-3.07 W/m²) $>$ winter (-1.94 W/m²). At the surface
531 (SFC), radiative forcing reaches a peak of -20 W/m² in the Tarim Basin and southwestern Central Asia.
532 Atmospheric shortwave radiative forcing aligns spatially with TOA and SFC patterns, peaking at 10.02
533 W/m² in spring, which correlates closely with the seasonal characteristics of dust activity.
534 Simulations using the SBDART model indicate that aerosol direct radiative forcing (ADRF) at the sites
535 peaks in summer at Dushanbe (56.72 W/m²), Issyk-Kul (34.22 W/m²), and Jinghe (61.17 W/m²),
536 declining to annual minima in winter (approximately 2.33 W/m² at Dushanbe and 27.36 W/m² at
537 Jinghe). At Kashgar, ADRF exhibits a distinct spring peak of 92.99 W/m². Variations in atmospheric
538 heating rates show a strong positive correlation with ADRF. Heating rate peaks occur during the active
539 dust season at all sites: summer at Dushanbe (1.29 K/day) and Jinghe (1.72 K/day), and spring at
540 Kashgar (2.61 K/day). Notably, the heating rate at Issyk-Kul is substantially lower in spring (0.08
541 K/day) than in autumn (0.34 K/day), reflecting seasonal modulation of dust emission intensity and the
542 influence of local boundary layer processes.

543 **4.2 Discussion**

544 **4.2.1 SARIMA Forecasting**

545 This study integrates MERRA-2 reanalysis data, CMIP6 multi-model ensemble (MME) simulations,
546 and ground-based sun photometer observations to develop a fully coupled “emission–deposition–
547 radiation” framework for the dust cycle in Central Asia, thereby systematically elucidating the radiative
548 regulatory mechanisms of dust aerosols on the land–atmosphere system. To address the pronounced
549 spatiotemporal heterogeneity in aerosol radiative forcing and the limitations of observational data, this
550 study employs a seasonal autoregressive integrated moving average (SARIMA) model. Leveraging
551 MERRA-2 reanalysis data and SBDART-derived site-level radiative forcing time series from 1980 to
552 2023, this approach facilitates short-term predictive analyses from local to regional scales.

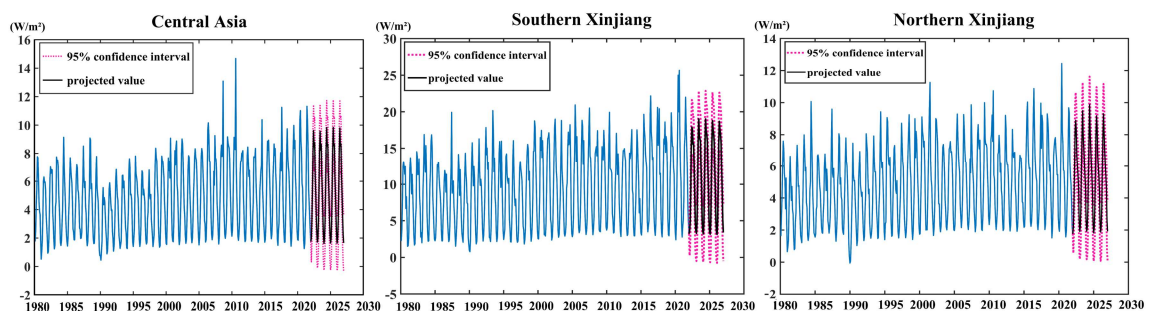
553 In contrast to century-scale CMIP6 scenario simulations, the SARIMA model quantifies the interannual
554 and short-term internal variability in dust radiative forcing (Kumar et al. 2018), enabling operational

555 forecasts for the next 5–10 years. This method is particularly well-suited for near-term predictions of
556 high-uncertainty variables, as it effectively captures seasonal and short-term fluctuations while
557 providing quantitative support for regional dust risk assessments and policy formulation.
558 Methodologically, it complements long-term model simulations by providing a near-term predictive
559 perspective(Mondal et al. 2025, Sami et al. 2012).

560 The forecast results (Figure 10) indicate that dust radiative forcing over the arid regions of Central Asia
561 during 2024–2029 exhibits an overall quasi-stationary pattern, with interannual fluctuations ranging
562 from 1.6 to 9.8 W/m² (peaking in 2026) and no indications of extreme events. Regional differences are
563 pronounced: southern Xinjiang represents a strong radiative response zone (2.8–18.9 W/m²), whereas
564 northern Xinjiang shows a non-stationary trend of initial increase followed by decline (1.6–10.0 W/m²),
565 likely reflecting the bidirectional modulation of dust emissions by changes in snow cover.

566 Model validation results (Supplementary Figure 11) confirm that the residuals of the
567 SARIMA(1,1,0)×(1,0,2)₁₂ model satisfy the white noise assumption (Ljung–Box Q test, $p > 0.05$) and
568 approximate normality (Kolmogorov–Smirnov test, $D = 0.12$), with autocorrelation coefficients falling
569 within the 95% confidence interval. Quantitative metrics of predictive performance include RMSE =
570 1.72 W/m², MAE = 1.21 W/m², MAPE = 8.6%, and $R^2 = 0.70$, demonstrating the model’s strong
571 capability for short-term predictions.

572 Thus, the SARIMA model serves as a methodological complement: it not only validates the internal
573 variability captured in reanalysis and observational time series but also provides operational forecasts
574 for near-future regional climate risk management. This short-term predictive approach complements
575 CMIP6 long-term simulations, bridging the gap between large-scale climate projections and near-term
576 adaptation needs.



577

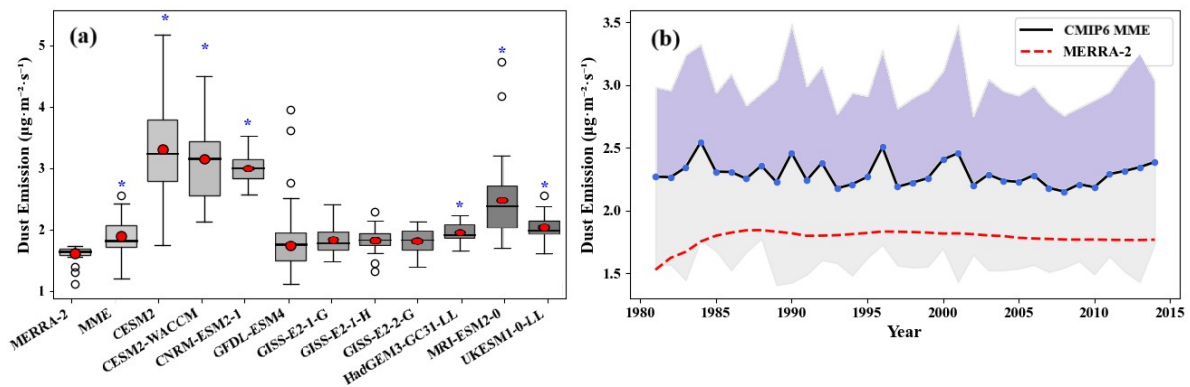
578

Figure.10 Dust aerosol direct radiative forcing SARIMA model predictions.

579 **4.2.2 Uncertainty Analysis**

580 The CMIP6 multi-model ensemble (MME) provides a robust analytical framework for assessing future
 581 variations in dust budgets across Central Asia. However, differences among models in dust emission
 582 parameterization, particle size distribution, and surface schemes introduce a degree of uncertainty in
 583 the simulations. To systematically evaluate these uncertainties and enhance the reliability of the results,
 584 this study employs complementary diagnostic approaches that quantify both inter-model variability and
 585 biases arising from the statistical downscaling procedure.

586 To assess inter-model dispersion, dust emissions from each model were compared with MERRA-2
 587 reanalysis data(Onyutha et al. 2016). As shown in Figure 10a, emission biases of individual models
 588 were evaluated using a two-tailed t-test ($p < 0.05$) to determine statistical significance. The results
 589 indicate that several models — including CESM2, CESM2-WACCM, CNRM-ESM2-1, and MRI-
 590 ESM2-1 — exhibit relatively large deviations, suggesting that their dust modules or physical
 591 parameterization schemes may introduce additional uncertainties. Figure 10b further illustrates the time
 592 series of dust emissions along with the $\pm 1\sigma$ inter-model variability (shaded area). Despite the
 593 dispersion among models, the MERRA-2 record consistently falls within the historical model range,
 594 indicating that the MME ensemble mean provides a reasonable representation of the climatological
 595 mean state and effectively captures the “three-source, high-emission” spatial pattern characteristic of
 596 Central Asia’s major dust source regions.

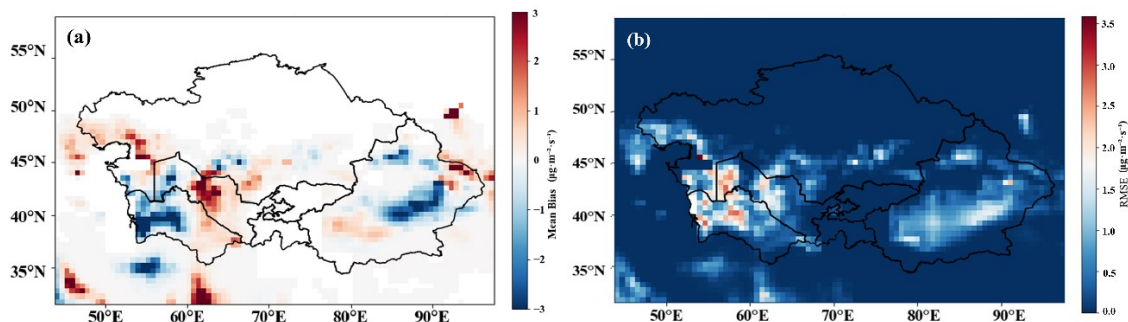


597 **Figure. 11 (a) Dust emission biases of individual models relative to MERRA-2 reanalysis data; (b)**
 598 **time series of dust emissions from the CMIP6 multi-model ensemble, with $\pm 1\sigma$ inter-model**
 599 **variability indicated by the shaded area.**

600 To further elucidate regional differences, Figure 11a and Supplementary Figure 12 depict the spatial
 601 bias distributions of individual models within the multi-model ensemble (MME). The results reveal
 602 that all models exhibit biases in key dust source regions, including the Taklamakan Desert, Kumtag

603 Desert, areas surrounding the Aral Sea, Karakum Desert, and the eastern Caspian Sea. Specifically,
 604 positive biases predominate in the southeastern Tarim Basin, whereas negative biases dominate in the
 605 western Karakum Desert and parts of the Aral Sea region.

606 The bias-corrected statistical downscaling method employed in this study, which relies on MERRA-2
 607 data, is well-suited to Central Asia's complex terrain and sparse observational networks. It offers low
 608 computational costs while preserving the statistical relationships between dust emissions and climate
 609 variables. However, its capacity to simulate extreme events and nonlinear processes (e.g., intense dust
 610 storms) remains limited. To quantify downscaling biases, Figure 12b illustrates the spatial root-mean-
 611 square error (RMSE) between CMIP6 downscaled outputs and MERRA-2 data. The results indicate
 612 higher RMSE values ($>2 \mu\text{g}\cdot\text{m}^{-2}\cdot\text{s}^{-1}$) in complex terrain regions, such as the Tarim Basin and Karakum
 613 Desert, suggesting that predictions in these areas should be interpreted with caution. Supplementary
 614 Figure 13 presents a scatterplot demonstrating a high correlation between downscaled MME changes
 615 (ΔMME) and MERRA-2 observations ($R^2 > 0.91$), although a slight underestimation bias is evident
 616 (Bias = -1.26 , RMSE = 4.31). The time series comparison in Supplementary Figure 13b further
 617 demonstrates that the downscaled results effectively capture seasonal and interannual
 618 variability. Overall, the multi-model ensemble, combined with bias-corrected downscaling,
 619 demonstrates reasonable robustness, providing a credible reference for assessing future dust changes in
 620 Central Asia.



621
 622 **Figure. 12 (a) Spatial distribution of biases between individual models in the multi-model**
 623 **ensemble and MERRA-2 reanalysis data; (b) spatial distribution of root-mean-square error**
 624 **(RMSE) between CMIP6 downscaled outputs and MERRA-2 reanalysis data.**

625 Although the results presented above provide multiple lines of evidence for understanding the dust
 626 cycle in Central Asia, their limitations cannot be overlooked. The dust budget encompasses key
 627 processes such as emission, transport, deposition, and mass loading. While previous studies have
 628 advanced our knowledge, achieving a comprehensive understanding of the complex interactions among

629 dust, land surface, vegetation, and climate remains a significant challenge. In particular, variability in
630 dust particle size assumptions across CMIP6 models markedly affects simulation consistency(Zhao,
631 Ryder and Wilcox 2022), thereby increasing uncertainty in representing dust cycle processes.
632 Second, although existing radiative transfer models such as SBDART are suitable for point-scale
633 simulations, they do not fully account for aerosol–cloud interactions, which are particularly important
634 in regions with high dust concentrations; neglecting this process may introduce biases in radiative
635 forcing estimates. The SBDART simulations in this study rely on a limited set of ground-based
636 observational sites in Central Asia, which, while representative in terms of geographic location and
637 underlying surface types, are sparsely distributed and thus capture only local responses at typical sites
638 rather than spatially averaged effects across the entire region. For example, the Ili Lake site exhibits
639 lower atmospheric heating rates in spring, likely attributable to data scarcity and the shielding effects of
640 complex mountainous terrain, underscoring the challenges of high-altitude observations.
641 Due to the sparse observational network, no weighting was applied to the sites; instead, they were
642 treated as independent case studies to highlight variability under different environmental conditions.
643 The representativeness of these sites is corroborated by cross-validation with MERRA-2 reanalysis
644 data (Supplementary Figure 1); however, they still cannot fully characterize the complex radiative
645 effects across Central Asia's extensive and heterogeneous landscapes.

646 **Author contributions**

647 All authors contributed to the manuscript and approved the final version. YG designed the study,
648 performed the data analysis, and wrote the original draft. WC, JD, and YR assisted with data collection
649 and software processing. YR also contributed to the validation and interpretation of results. ZZ
650 supervised the research and contributed to manuscript revision and funding acquisition.

651 **Competing interests.**

652 The contact author has declared that none of the authors has any competing interests.

653 **Funding**

654 Open Project of Key Laboratory in Xinjiang Uygur Autonomous Region of China (2023D04066),

655 National Natural Science Foundation of China (No. 42061066), and Xinjiang University Outstanding
656 Graduate Student Innovation Program(XJDX2025YJS065).

657 **Acknowledgements**

658 We are sincerely grateful to MERRA-2 (<https://gmao.gsfc.nasa.gov/reanalysis/MERRA-2/>),
659 CMIP6 (<https://esgf-node.ipsl.upmc.fr/projects/cmip6-ipsi/>), AERONET and SONET Instrument
660 Science Teams for providing the datasets, which are available on the Web and constitute the
661 centralized database for the current work. We thank the faculty members who worked hard to
662 review this thesis.

663 **References:**

- 664 Braconnot, P., Albani, S., Balkanski, Y., Cozic, A., Kageyama, M., Sima, A., Marti, O., and
665 Peterschmitt, J.-Y.: Impact of dust in PMIP-CMIP6 mid-Holocene simulations with the IPSL
666 model, *Clim. Past*, 17, 1091–1117, <https://doi.org/10.5194/cp-17-1091-2021>, 2021.
- 667 Brown, H., Liu, X., Pokhrel, R., Murphy, S., Lu, Z., Saleh, R., Mielonen, T., Kokkola, H.,
668 Bergman, T., and Myhre, G.: Biomass burning aerosols in most climate models are too absorbing,
669 *Nat. Commun.*, 12, 277, <https://doi.org/10.1038/s41467-020-20482-9>, 2021.
- 670 Buchard, V., Randles, C. A., da Silva, A. M., Darmenov, A., Colarco, P. R., Govindaraju, R.,
671 Ferrare, R., Hair, J., Beyersdorf, A. J., and Ziemba, L. D.: The MERRA-2 aerosol reanalysis, 1980
672 onward. Part II: Evaluation and case studies, *J. Climate*, 30, 6851–6872,
673 <https://doi.org/10.1175/JCLI-D-16-0613.1>, 2017.
- 674 Chen, A., Zhao, C., and Fan, T.: Spatio-temporal distribution of aerosol direct radiative forcing
675 over mid-latitude regions in north hemisphere estimated from satellite observations, *Atmos. Res.*,
676 266, 105938, <https://doi.org/10.1016/j.atmosres.2021.105938>, 2022.
- 677 Dai, Y., Hitchcock, P., Mahowald, N. M., Domeisen, D. I. V., Hamilton, D. S., Li, L., Marticorena,
678 B., Kanakidou, M., Mihalopoulos, N., and Aboagye-Okyere, A.: Stratospheric impacts on dust
679 transport and air pollution in West Africa and the Eastern Mediterranean, *Nat. Commun.*, 13, 7744,
680 <https://doi.org/10.1038/s41467-022-35403-1>, 2022.
- 681 Dubovik, O. and King, M. D.: A flexible inversion algorithm for retrieval of aerosol optical

682 properties from Sun and sky radiance measurements, *J. Geophys. Res. Atmos.*, 105, 20673–20696,
683 <https://doi.org/10.1029/2000JD900282>, 2000.

684 Eyring, V., Bony, S., Meehl, G. A., Senior, C. A., Stevens, B., Stouffer, R. J., and Taylor, K. E.:
685 Overview of the Coupled Model Intercomparison Project Phase 6 (CMIP6) experimental design
686 and organization, *Geosci. Model Dev.*, 9, 1937–1958, <https://doi.org/10.5194/gmd-9-1937-2016>,
687 2016.

688 Fu, A., Li, W., Chen, Y., Wang, Y., Hao, H., Li, Y., Sun, F., Zhou, H., Zhu, C., and Hao, X.: The
689 effects of ecological rehabilitation projects on the resilience of an extremely drought-prone desert
690 riparian forest ecosystem in the Tarim River Basin, Xinjiang, China, *Sci. Rep.*, 11, 18485,
691 <https://doi.org/10.1038/s41598-021-96742-5>, 2021.

692 García, O. E., Díaz, J. P., Expósito, F. J., Díaz, A. M., Dubovik, O., Derimian, Y., Dubuisson, P.,
693 and Roger, J.-C.: Shortwave radiative forcing and efficiency of key aerosol types using
694 AERONET data, *Atmos. Chem. Phys.*, 12, 5129–5145, <https://doi.org/10.5194/acp-12-5129-2012>,
695 2012.

696 Gelaro, R., McCarty, W., Suárez, M. J., Todling, R., Molod, A., Takacs, L., Randles, C. A.,
697 Darmenov, A., Bosilovich, M. G., Reichle, R., and co-authors: The Modern-Era Retrospective
698 Analysis for Research and Applications, version 2 (MERRA-2), *J. Climate*, 30, 5419–5454,
699 <https://doi.org/10.1175/JCLI-D-16-0758.1>, 2017.

700 Gutmann, E., Pruitt, T., Clark, M. P., Brekke, L., Arnold, J. R., Raff, D. A., and Rasmussen, R. M.:
701 An intercomparison of statistical downscaling methods used for water resource assessments in the
702 United States, *Water Resour. Res.*, 50, 7167–7186, <https://doi.org/10.1002/2014WR015559>, 2014.

703 Halthore, R. N., Crisp, D., Schwartz, S. E., Anderson, G. P., Berk, A., Bonnel, B., Boucher, O.,
704 Chang, F.-L., Chou, M.-D., Clothiaux, E. E., and co-authors: Intercomparison of shortwave
705 radiative transfer codes and measurements, *J. Geophys. Res. Atmos.*, 110, D11206,
706 <https://doi.org/10.1029/2004JD005293>, 2005.

707 Heald, C. L., Ridley, D. A., Kroll, J. H., Barrett, S. R. H., Cady-Pereira, K. E., Alvarado, M. J.,
708 and Holmes, C. D.: Contrasting the direct radiative effect and direct radiative forcing of aerosols,
709 *Atmos. Chem. Phys.*, 14, 5513–5527, <https://doi.org/10.5194/acp-14-5513-2014>, 2014.

710 Hetzel, R., Niedermann, S., Tao, M., Kubik, P. W., Ivy-Ochs, S., Gao, B., and Strecker, M. R.:

711 Low slip rates and long-term preservation of geomorphic features in Central Asia, *Nature*, 417,
712 428–432, <https://doi.org/10.1038/417428a>, 2002.

713 Holben, B. N., Eck, T. F., Slutsker, I., Tanré, D., Buis, J. P., Setzer, A., Vermote, E., Reagan, J. A.,
714 Kaufman, Y. J., Nakajima, T., and co-authors: AERONET—A federated instrument network and
715 data archive for aerosol characterization, *Remote Sens. Environ.*, 66, 1–16,
716 [https://doi.org/10.1016/S0034-4257\(98\)00031-5](https://doi.org/10.1016/S0034-4257(98)00031-5), 1998.

717 Holben, B. N., Tanré, D., Smirnov, A., Eck, T. F., Slutsker, I., Abuhassan, N., Newcomb, W. W.,
718 Schafer, J. S., Chatenet, B., Lavenu, F., and co-authors: An emerging ground-based aerosol
719 climatology: Aerosol optical depth from AERONET, *J. Geophys. Res. Atmos.*, 106, 12067–12097,
720 <https://doi.org/10.1029/2001JD900014>, 2001.

721 IPCC: Climate Change 2021: The Physical Science Basis. Contribution of Working Group I to the
722 Sixth Assessment Report of the Intergovernmental Panel on Climate Change, edited by: Masson-
723 Delmotte, V., Zhai, P., Pirani, A., Connors, S. L., Péan, C., Berger, S., Caud, N., Chen, Y.,
724 Goldfarb, L., Gomis, M. I., Huang, M., Leitzell, K., Lonnoy, E., Matthews, J. B. R., Maycock, T.
725 K., Waterfield, T., Yelekçi, O., Yu, R., and Zhou, B., Cambridge University Press, Cambridge,
726 United Kingdom and New York, NY, USA, 2391 pp., <https://doi.org/10.1017/9781009157896>,
727 2021.

728 Kok, J. F., Storelvmo, T., Karydis, V. A., Adebisi, A. A., Mahowald, N. M., Evan, A. T., He, C.,
729 and Leung, D. M.: Mineral dust aerosol impacts on global climate and climate change, *Nat. Rev.*
730 *Earth Environ.*, 4, 71–86, <https://doi.org/10.1038/s43017-022-00379-5>, 2023.

731 Li, J., Carlson, B. E., Yung, Y. L., Lv, D., Hansen, J., Penner, J. E., Liao, H., Ramaswamy, V.,
732 Kahn, R. A., Zhang, P., and co-authors: Scattering and absorbing aerosols in the climate system,
733 *Nat. Rev. Earth Environ.*, 3, 363–379, <https://doi.org/10.1038/s43017-022-00296-7>, 2022a.

734 Li, X., Dong, X., Liu, Y., Wang, M., Jiang, Y., and Dong, Y.: Assessment of the Coupled Model
735 Intercomparison Project phase 6 (CMIP6) model performance in simulating the spatial-temporal
736 variation of aerosol optical depth over Eastern Central China, *Atmos. Res.*, 261, 105747,
737 <https://doi.org/10.1016/j.atmosres.2021.105747>, 2021.

738 Li, Y., Song, Y., Kaskaoutis, D. G., Zhang, X., Chen, X., Shukurov, N., and Orozbaev, R.:
739 Atmospheric dust dynamics over Central Asia: A perspective view from loess deposits, *Gondwana*

740 Res., 109, 150–165, <https://doi.org/10.1016/j.gr.2022.04.019>, 2022b.

741 Li, Z., Xu, H., Li, K. T., Li, D., Xie, Y., Li, L., Zhang, Y., Gu, X., Zhao, W., Tian, Q., and co-
742 authors: Comprehensive study of optical, physical, chemical, and radiative properties of total
743 columnar atmospheric aerosols over China: An overview of Sun–Sky Radiometer Observation
744 Network (SONET) measurements, *Bull. Am. Meteorol. Soc.*, 99, 739–755,
745 <https://doi.org/10.1175/BAMS-D-17-0133.1>, 2018.

746 Lioubimtseva, E. and Cole, R.: Uncertainties of climate change in arid environments of Central
747 Asia, *Rev. Fish. Sci.*, 14, 29–49, <https://doi.org/10.1080/10641260500340603>, 2006.

748 Liu, J., Wang, X., Wu, D., Wei, H., Li, Y., and Ji, M.: Historical footprints and future projections
749 of global dust burden from bias-corrected CMIP6 models, *npj Clim. Atmos. Sci.*, 7, 1,
750 <https://doi.org/10.1038/s41612-023-00550-9>, 2024.

751 Mahowald, N. M., Kloster, S., Engelstaedter, S., Moore, J. K., Mukhopadhyay, S., McConnell, J.
752 R., Albani, S., Doney, S. C., Bhattacharya, A., Curran, M. A. J., and co-authors: Observed 20th
753 century desert dust variability: impact on climate and biogeochemistry, *Atmos. Chem. Phys.*, 10,
754 10875–10893, <https://doi.org/10.5194/acp-10-10875-2010>, 2010.

755 Maraun, D., Wetterhall, F., Ireson, A. M., Chandler, R. E., Kendon, E. J., Widmann, M., Brienen,
756 S., Rust, H. W., Sauter, T., Themeßl, M., and co-authors: Precipitation downscaling under climate
757 change: Recent developments to bridge the gap between dynamical models and the end user, *Rev.*
758 *Geophys.*, 48, RG3003, <https://doi.org/10.1029/2009RG000314>, 2010.

759 Marticorena, B. and Bergametti, G.: Modeling the atmospheric dust cycle: 1. Design of a soil-
760 derived dust emission scheme, *J. Geophys. Res. Atmos.*, 100, 16415–16430,
761 <https://doi.org/10.1029/95JD00690>, 1995.

762 Nakamae, K. and Takemi, T.: Relationship between the development of a convective mixed layer
763 and dust weather in arid and semi-arid regions of East Asia, *Int. J. Climatol.*, 42, 3076–3093,
764 <https://doi.org/10.1002/joc.7373>, 2022.

765 Penner, J. E., Quaas, J., Storelvmo, T., Takemura, T., Boucher, O., Guo, H., Kirkevåg, A.,
766 Kristjánsson, J. E., and Seland, Ø.: Model intercomparison of indirect aerosol effects, *Atmos.*
767 *Chem. Phys.*, 6, 3391–3405, <https://doi.org/10.5194/acp-6-3391-2006>, 2006.

768 Pozzer, A., de Meij, A., Pringle, K. J., Tost, H., Doering, U. M., van Aardenne, J., and Lelieveld, J.:

769 Distributions and regional budgets of aerosols and their precursors simulated with the EMAC
770 chemistry-climate model, *Atmos. Chem. Phys.*, 12, 961–987, [https://doi.org/10.5194/acp-12-961-](https://doi.org/10.5194/acp-12-961-2012)
771 [2012](https://doi.org/10.5194/acp-12-961-2012), 2012.

772 Rupakheti, D., Rupakheti, M., Rai, M., Yin, X., Hofer, J., Hu, Y., Abdullaev, S. F., Kang, S., and
773 Lawrence, M. G.: Characterization of columnar aerosol over a background site in Central Asia,
774 *Environ. Pollut.*, 316, 120501, <https://doi.org/10.1016/j.envpol.2022.120501>, 2023.

775 Ramanathan, V., Crutzen, P. J., Kiehl, J. T., and Rosenfeld, D.: Aerosols, climate, and the
776 hydrological cycle, *Science*, 294, 2119–2124, <https://doi.org/10.1126/science.1064034>, 2001.

777 Ricchiazzi, P., Yang, S., Gautier, C., and Sowle, D.: SBDART: A research and teaching software
778 tool for plane-parallel radiative transfer in the Earth's atmosphere, *Bull. Am. Meteorol. Soc.*, 79,
779 2101–2114, [https://doi.org/10.1175/1520-0477\(1998\)079<2101:SARATS>2.0.CO;2](https://doi.org/10.1175/1520-0477(1998)079<2101:SARATS>2.0.CO;2), 1998.

780 Salvador, P., Pey, J., Pérez, N., Querol, X., and Artíñano, B.: Increasing atmospheric dust transport
781 towards the western Mediterranean over 1948–2020, *npj Clim. Atmos. Sci.*, 5, 34,
782 <https://doi.org/10.1038/s41612-022-00255-9>, 2022.

783 Shao, Y., Wyrwoll, K.-H., Chappell, A., Huang, J., Lin, Z., McTainsh, G. H., Mikami, M., Tanaka,
784 T. Y., Wang, X., and Yoon, S.: Dust cycle: An emerging core theme in Earth system science,
785 *Aeolian Res.*, 2, 181–204, <https://doi.org/10.1016/j.aeolia.2011.02.001>, 2011.

786 She, L., Li, Z., de Leeuw, G., Wang, Y., Wang, L., Yang, Z., Feng, C., Yang, C., and Shi, Y.: Time
787 series retrieval of multi-wavelength aerosol optical depth by adapting Transformer (TMAT) using
788 Himawari-8 AHI data, *Remote Sens. Environ.*, 305, 114115,
789 <https://doi.org/10.1016/j.rse.2024.114115>, 2024.

790 Shen, H., Abuduwaili, J., Samat, A., and Ma, L.: A review on the research of modern aeolian dust
791 in Central Asia, *Arab. J. Geosci.*, 9, 326, <https://doi.org/10.1007/s12517-016-2354-9>, 2016.

792 Sirisha, U. M., Belavagi, M. C., and Attigeri, G.: Profit prediction using ARIMA, SARIMA and
793 LSTM models in time series forecasting: A comparison, *IEEE Access*, 10, 124715–124727,
794 <https://doi.org/10.1109/ACCESS.2022.3223274>, 2022.

795 Sokolik, I. N. and Toon, O. B.: Direct radiative forcing by anthropogenic airborne mineral
796 aerosols, *Nature*, 381, 681–683, <https://doi.org/10.1038/381681a0>, 1996.

797 Song, Q., Zhang, Z., Yu, H., Ginoux, P., and Shen, J.: Global dust optical depth climatology

798 derived from CALIOP and MODIS aerosol retrievals on decadal timescales: regional and
799 interannual variability, *Atmos. Chem. Phys.*, 21, 13369–13395, [https://doi.org/10.5194/acp-21-](https://doi.org/10.5194/acp-21-13369-2021)
800 [13369-2021](https://doi.org/10.5194/acp-21-13369-2021), 2021.

801 Tanaka, T. Y. and Chiba, M.: A numerical study of the contributions of dust source regions to the
802 global dust budget, *Global Planet. Change*, 52, 88–104,
803 <https://doi.org/10.1016/j.gloplacha.2006.02.002>, 2006.

804 Tao, M., Chen, L., Wang, J., Wang, L., Wang, W., Lin, C., Gui, L., Wang, C., Yu, C., and Wang, Y.:
805 Characterization of dust activation and their prevailing transport over East Asia based on multi-
806 satellite observations, *Atmos. Res.*, 265, 105886, <https://doi.org/10.1016/j.atmosres.2021.105886>,
807 2022.

808 Tegen, I., Werner, M., Harrison, S. P., and Kohfeld, K. E.: Relative importance of climate and land
809 use in determining present and future global soil dust emission, *Geophys. Res. Lett.*, 31, L05105,
810 <https://doi.org/10.1029/2003GL019216>, 2004.

811 Wallace, J. M. and Hobbs, P. V.: *Atmospheric science: an introductory survey*, 2nd edn., Academic
812 Press, Amsterdam, 483 pp., 2006.

813 Wang, X., Chen, Y., Li, Z., Fang, G., Wang, F., and Liu, H.: The impact of climate change and
814 human activities on the Aral Sea Basin over the past 50 years, *Atmos. Res.*, 245, 105125,
815 <https://doi.org/10.1016/j.atmosres.2020.105125>, 2020.

816 Wang, X., Liu, J., Che, H., Ji, F., and Liu, J.: Spatial and temporal evolution of natural and
817 anthropogenic dust events over northern China, *Sci. Rep.*, 8, 2141, [https://doi.org/10.1038/s41598-](https://doi.org/10.1038/s41598-018-20357-3)
818 [018-20357-3](https://doi.org/10.1038/s41598-018-20357-3), 2018.

819 Wang, Z., Lin, L., Xu, Y., Che, H., Zhang, X., Zhang, H., Dong, W., Wang, C., Gui, K., and Xie,
820 B.: Incorrect Asian aerosols affecting the attribution and projection of regional climate change in
821 CMIP6 models, *npj Clim. Atmos. Sci.*, 4, 2, <https://doi.org/10.1038/s41612-020-00159-3>, 2021.

822 Wu, T. and Boor, B. E.: Urban aerosol size distributions: a global perspective, *Atmos. Chem. Phys.*,
823 21, 8883–8914, <https://doi.org/10.5194/acp-21-8883-2021>, 2021.

824 Xu, M., Wang, X., Sun, T., Wu, H., Li, X., and Kang, S.: Water balance change and its
825 implications to vegetation in the Tarim River Basin, Central Asia, *Quat. Int.*, 523, 25–36,
826 <https://doi.org/10.1016/j.quaint.2019.05.008>, 2019.

827 Zhang, X.-X., Claiborn, C., Lei, J.-Q., Vaughan, J., Wu, S.-X., Li, S.-Y., Liu, L.-Y., Wang, Z.-F.,
828 Wang, Y.-D., Huang, S.-Y., and co-authors: Aeolian dust in Central Asia: spatial distribution and
829 temporal variability, *Atmos. Environ.*, 238, 117734,
830 <https://doi.org/10.1016/j.atmosenv.2020.117734>, 2020.

831 Zhao, A., Ryder, C. L., and Wilcox, L. J.: How well do the CMIP6 models simulate dust aerosols?,
832 *Atmos. Chem. Phys.*, 22, 2095–2119, <https://doi.org/10.5194/acp-22-2095-2022>, 2022.

833 Zhao, A., Wilcox, L. J., and Ryder, C. L.: The key role of atmospheric absorption in the Asian
834 summer monsoon response to dust emissions in CMIP6 models, *Atmos. Chem. Phys.*, 24, 13385–
835 13402, <https://doi.org/10.5194/acp-24-13385-2024>, 2024.

836 Zhao, Y., Yue, X., Cao, Y., Zhu, J., Tian, C., Zhou, H., Chen, Y., Hu, Y., Fu, W., and Zhao, X.:
837 Multi-model ensemble projection of the global dust cycle by the end of 21st century using the
838 Coupled Model Intercomparison Project version 6 data, *Atmos. Chem. Phys.*, 23, 7823–7838,
839 <https://doi.org/10.5194/acp-23-7823-2023>, 2023.

840